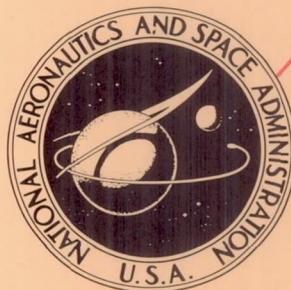


NASA TECHNICAL NOTE



N63-23652

NASA TN D-2017

NASA TN D-2017

FLIGHT TEST AND ANALYSIS OF THE
ROLLING MOTIONS OF A 79° CLIPPED
DELTA CONFIGURATION WITH WING-TIP
FINS AT SUPERSONIC SPEEDS

by James L. Raper
Langley Research Center
Langley Station, Hampton, Va.

NATIONAL AERONAUTICS AND SPACE ADMINISTRATION

TECHNICAL NOTE D-2017

FLIGHT TEST AND ANALYSIS OF THE ROLLING MOTIONS
OF A 79° CLIPPED DELTA CONFIGURATION WITH
WING-TIP FINS AT SUPERSONIC SPEEDS

By James L. Raper

SUMMARY

A free-flight investigation was conducted to determine the aerodynamic characteristics and motions of a rocket-boosted model of a simplified hypersonic glider configuration with wing-tip fins and a blunt base through a Mach number range extending up to 4.4. The model was statically and dynamically stable at small angles of attack and experienced coupled motions when pitched to an angle of attack of about 12° . The addition of the wing-tip fins resulted in no improvement of the vehicle motions compared with the same vehicle with no fins.

In general, the coupled motions experienced by the model were simulated by the use of the equations of motion for five degrees of freedom. The analog study showed that the rate of change of effective-dihedral derivative with change in angle of attack was a significant cross-coupling derivative for the configuration studied and should be considered for flight prediction of the motions for configurations which are highly swept and have the mass concentrated along the longitudinal axis. An analytical solution for a simplified three-degree-of-freedom set of equations yielded results that compared satisfactorily with the flight records of rolling velocity and yielded a rolling velocity parameter which affected the type of rolling motion experienced. The appendix presents the analytical solution.

INTRODUCTION

The current interest in highly swept, delta wing configurations for high-speed reentry and manned orbital flight has prompted a free-flight investigation to determine the aerodynamic characteristics and dynamic behavior of several research models with these general characteristics. Reference 1 presents the results of one such test and shows that the model angular velocities became large and erratic following a disturbance. The rolling velocities were of particular interest, with periodic positive and negative values along with short-period sinusoidal-like peak-magnitude variations of 35 radians per second being experienced. Electronic analog motion simulation showed that the primary reason for

this behavior was the concentration of mass along the axis of symmetry, the low roll inertia, and the large increase in rolling moment due to sideslip with increasing angle of attack.

The object of this investigation is to present the dynamic behavior of a delta wing configuration which is the same as that of reference 1, except for the addition of wing-tip fins which were added with the idea of increasing directional stability, of reducing coupling forces, and hence, it was thought, of decreasing the roll rates and accelerations.

The model was flight tested at the NASA Wallops Station over a Mach number range from 4.4 to approximately 1.5 with corresponding Reynolds numbers, based on wing mean aerodynamic chord, of 42.5×10^6 and 0.7×10^6 . Pulse rockets were used to disturb the model in pitch to an angle of attack of about 12° , and a 10-channel telemeter was used to transmit continuous acceleration and pressure data to ground receiving stations.

Aerodynamic coefficients based on accelerations of the center of gravity are presented. With the use of five-degree-of-freedom equations of motion, an analysis of the rolling motions was made by comparing the free-flight data with analog runs for similar altitude and aerodynamic-coefficient conditions. In addition, an analytical solution of a simplified set of three-degree-of-freedom equations of motion were used to predict rolling motions.

SYMBOLS

The basic data in this report are presented with respect to an axis system originating at the 54.3-percent station on the longitudinal axis of the rocket model. (See fig. 1.)

$a_{L, cg}$	longitudinal accelerometer reading referenced to center of gravity, g units
$a_{L, Hi}$	high-range longitudinal accelerometer reading, positive in positive x-direction, g units
$a_{L, Lo}$	low-range longitudinal accelerometer reading, positive in positive x-direction, g units
$a_{N, cg}$	normal accelerometer reading referenced to center of gravity, g units
$a_{N, n}$	normal accelerometer reading at nose location, positive in negative z-direction, g units
$a_{N, t}$	normal accelerometer reading at tail location, positive in negative z-direction, g units
a_y	lateral accelerometer reading, positive in positive y-direction, g units

$a_{Y, cg}$	lateral accelerometer reading referenced to center of gravity, g units
b	wing span, 1.77 ft
C_D	drag coefficient, $\frac{\text{Drag}}{q_\infty S}$
C_L	lift coefficient, $C_L \approx C_N \cos \alpha$, $\frac{\text{Lift}}{q_\infty S}$
$C_{L\alpha}$	lift-coefficient derivative, $\frac{\partial C_L}{\partial \alpha}$, per radian
C_l	rolling-moment coefficient, $\frac{\text{Rolling moment}}{q_\infty S b}$
C_{lp}	damping-in-roll derivative, $\frac{\partial C_l}{\partial \left(\frac{pb}{2V}\right)}$, per radian
C_{lr}	rate of change of rolling-moment coefficient with change in yawing angular velocity factor, $\frac{\partial C_l}{\partial \left(\frac{rb}{2V}\right)}$, per radian
$C_{l\beta}$	effective-dihedral derivative, $\frac{\partial C_l}{\partial \beta}$, per radian
$C_{l\beta\alpha}$	rate of change of effective-dihedral derivative with change in angle of attack, $\frac{\partial C_{l\beta}}{\partial \alpha}$, per square radian
C_m	pitching-moment coefficient, $\frac{\text{Pitching moment}}{q_\infty S \bar{c}}$
C_{mq}	rate of change of pitching-moment coefficient with pitching angular velocity parameter, $\frac{\partial C_m}{\partial \left(\frac{q\bar{c}}{2V}\right)}$, per radian
$C_{m\alpha}$	static stability derivative, $\frac{\partial C_m}{\partial \alpha}$, per radian
$C_{m\dot{\alpha}}$	rate of change of pitching-moment coefficient with rate of change of angle-of-attack parameter, $\frac{\partial C_m}{\partial \left(\frac{\dot{\alpha}\bar{c}}{2V}\right)}$, per radian

- $C_{m\beta}$ rate of change of pitching-moment coefficient with angle of sideslip,
 $\frac{\partial C_m}{\partial \beta}$, per radian
- C_N normal-force coefficient, $\frac{\text{Normal force}}{q_\infty S}$
- $C_{N\alpha}$ normal-force-coefficient derivative, $\frac{\partial C_N}{\partial \alpha}$, per radian
- C_n yawing-moment coefficient, $\frac{\text{Yawing moment}}{q_\infty S b}$
- C_{np} rate of change of yawing-moment coefficient with rolling angular
velocity parameter, $\frac{\partial C_n}{\partial \left(\frac{pb}{2V}\right)}$, per radian
- C_{nr} rate of change of yawing-moment coefficient with yawing angular
velocity parameter, $\frac{\partial C_n}{\partial \left(\frac{rb}{2V}\right)}$, per radian
- $C_{n\beta}$ directional-stability derivative, $\frac{\partial C_n}{\partial \beta}$, per radian
- $C_{n\dot{\beta}}$ rate of change of yawing-moment coefficient with rate of change of
angle-of-sideslip parameter, $\frac{\partial C_n}{\partial \left(\frac{\dot{\beta} b}{2V}\right)}$, per radian
- $C_o = - \frac{q_\infty S b}{I_X} C_{l_{\beta\alpha}} \sigma_o^2$
- C_X axial-force coefficient, positive in positive x-direction, $\frac{\text{Axial force}}{q_\infty S}$
- C_Y lateral-force coefficient, $\frac{\text{Lateral force}}{q_\infty S}$
- C_{Yr} rate of change of side-force coefficient with angular velocity factor
in yaw, $\frac{\partial C_Y}{\partial \left(\frac{rb}{2V}\right)}$, per radian
- $C_{Y\beta}$ lateral-force-coefficient derivative, $\frac{\partial C_Y}{\partial \beta}$, per radian

\bar{c}	wing mean aerodynamic chord, 3.83 ft
F,K	incomplete and complete elliptic functions of first kind
g	acceleration due to gravity, 32.2 ft/sec ²
h	model altitude, ft
I _X	mass moment of inertia in roll, (slugs)(sq ft)
I _Y	mass moment of inertia in pitch, (slugs)(sq ft)
I _Z	mass moment of inertia in yaw, (slugs)(sq ft)
k	critical roll-rate parameter (eqs. (A14) and (A23))
l	reference length, ft
M	Mach number
m	model reference mass, W/g, slugs
p	rolling angular velocity, radians/sec
p _b	base pressure, lb/sq in.
p ₀	total pressure, measured at nose stagnation point, lb/sq in.
p _∞	free-stream pressure, lb/sq in.
q	pitching angular velocity, radians/sec
q _∞	free-stream dynamic pressure, $\frac{\rho V^2}{2}$, lb/sq ft
R	Reynolds number, based on wing mean aerodynamic chord (3.83 ft), $\frac{\rho V l}{\mu}$
r	yawing angular velocity, radians/sec
S	wing reference area, 5.87 sq ft
t	time, sec
V	velocity, ft/sec
W	model weight, lb
X,Y,Z	fixed body-axis system
x,y,z	distances measured along the X-, Y-, and Z-axes

α angle of attack, radians
 β angle of sideslip, radians
 γ flight-path angle referenced to local horizontal, deg
 μ free-stream coefficient of viscosity, lb-sec/sq ft
 ρ free-stream density, slugs/cu ft

$$\sigma_0 = \sqrt{\alpha_0^2 + \beta_0^2}$$

ϕ angle of roll, radians

$$\psi = \sin^{-1}(k \sin \phi)$$

Subscripts:

min minimum value
 max maximum value
 o initial condition

A dot (·) over a symbol denotes a first derivative with respect to time, and double dots (··) over a symbol denote a second derivative with respect to time. A bar (¯) indicates an angle normalized with respect to σ_0 .

MODEL AND INSTRUMENTATION

Model

A dimensional drawing of the rocket-boosted model is shown in figure 2. The reference areas and lengths and physical characteristics of the model are given in table I. Photographs of the model are presented in figure 3, and a photograph of the model and booster in launch position is shown in figure 4.

The model had planar symmetry in the horizontal and vertical planes, sharp leading edges, and a blunt trailing edge. The planform of the basic body was a 78.87° sweptback clipped delta surface with streamwise tips, aspect ratio of 0.53, and a taper ratio of 0.191. The wing-tip fins were clipped delta surfaces swept back 70°. The vertical tail had a sweepback angle of 76°. The planar surfaces of the model were not properly aligned in some instances because of tolerances of construction giving rise to slight aerodynamic asymmetries. A detailed description is presented in table I and figure 2 of the physical and mass characteristics of the complete model and of each component. For all practical purposes, the mass balance of the model was such that the principal axes were coincident with the body axes of symmetry.

Instrumentation

The rocket-boasted model was equipped with a 10-channel telemeter which continuously transmitted information concerning longitudinal, transverse, and normal acceleration; angular acceleration in pitch and yaw; angular velocity in roll; and total and base pressures. There were two longitudinal accelerometers, one with a g-unit range from 1 to -12 and one with a g-unit range from 1 to -2. There were also two normal accelerometers, one mounted in the nose section of the model, and the other mounted in the rear of the model. The base pressure data represented an average over the semispan of the blunt trailing edge of the model as obtained by a manifolded tube, as shown in figures 2 and 3(b). The locations of the instruments with respect to the center of gravity are given in table II.

The data accuracy of the 10 instruments installed in the rocket-propelled model was approximately ± 5 percent of the calibrated scale of each instrument. The error in the aerodynamic coefficients was dependent on the free-stream dynamic pressure, which had a possible variation of 25 percent, on velocity, which had possible variations of ± 100 feet per second, and on density, which had possible variations of ± 5 percent.

TESTS

Figure 4 is a photograph of the rocket model and launch vehicle elevated on the launcher prior to firing at the NASA Wallops Station. The three-stage launch vehicle consisted of an Honest John rocket with four standard 12-square-foot trapezoidal fins for a ground-fired first stage; a Nike M5 rocket motor with four standard 5-square-foot trapezoidal fins for a delayed, ground-fired second stage; and a Nike with four standard 5-square-foot 4° wedge fins for a ground initiated, timer-fired third stage.

A small pancake rocket motor was installed in the base of the model behind the blowout diaphragm (see fig. 3(b)) and was programed to separate the model from the burned-out third-stage Nike. Preflight calculations of the relative decelerations of the burned-out third-stage Nike and the model, based on drag-weight ratios, indicated the need for an additional separation force in order to prevent collision after separation. In order that this requirement be satisfied, two 3.25-inch Mk 7 rocket motors were strapped in reverse thrust position to the forward end of the third-stage Nike, as shown in figure 4. The nozzles of the two rocket motors were canted out 20° with respect to the center line of the third stage and were plugged and sealed to protect the grain and igniters from aerodynamic heating during the boosted portion of the flight.

Two pulse rockets with 27 pound-seconds of impulse (burning time 0.05 second) were located in the nose section of the model (see fig. 2) and so oriented that the direction of thrust was in the positive and negative z-directions. Approximate calculations prior to the free-flight test for which two-degree-of-freedom pitch-plane dynamics and aerodynamic coefficients from reference 2 were used indicated that the maximum disturbance in the pitch plane alone would be about 12° .

Continuous flight-path data were obtained by tracking the model with three radar sets: an AN/FPS-16, an SCR-584, and an SCR-584 Model II. Atmospheric conditions were obtained from a Rawinsonde balloon which was released prior to launch. Mach number and dynamic pressure were determined from the total pressure measurements of the model and the ambient pressures and temperatures at corresponding altitudes along the flight path. The error of the most accurate tracking radar set used (AN/FPS-16) was 0.1 mil for the given angular measurement and 50 feet for the given linear measurement.

Data are presented in this report ranging from a Mach number of about 4.4 at an altitude of about 34,000 feet to a Mach number of 1.1 at an altitude of about 108,000 feet. The variation of altitude with Mach number is presented in figure 5. Variations of dynamic pressure and Reynolds number with Mach number are presented in figures 6 and 7, respectively.

Plots of 10 channels of telemeter data, dynamic pressure, and Mach number for three time intervals of the flight test of the model are presented in figure 8. The points were machine plotted from magnetic tape records and show occasional scatter points due to noise. Figure 9 presents an envelope of the variation of maximum roll rates plotted against Mach number for the flight.

ANALYSIS

Basic Data Reduction

The measured free-flight linear-acceleration data were corrected to the center of gravity because linear accelerometers which are not mounted on the center of gravity measure not only the translatory accelerations but also the accelerations due to angular velocities and angular accelerations. The following relationships were used to correct the accelerometer readings to the center of gravity:

$$a_{L, cg} = a_{L, Lo} + \frac{1}{g} \left[x_{aL, Lo} (q^2 + r^2) + y_{aL, Lo} (\dot{r} - pq) - z_{aL, Lo} (\dot{q} + pr) \right] \quad (1)$$

$$a_{Y, cg} = a_Y + \frac{1}{g} \left[y_{aY} (r^2 + p^2) + z_{aY} (\dot{p} - qr) - x_{aY} (\dot{r} + pq) \right] \quad (2)$$

and

$$a_{N, cg} = a_{N, n} + \frac{1}{g} \left[-z_{aN, n} (p^2 + q^2) - x_{aN, n} (\dot{q} - pr) + y_{aN, n} (\dot{p} + qr) \right] \quad (3)$$

where the distances x , y , and z from the center of gravity to the individual accelerometer are given in table II. The variations of \dot{q} , \dot{r} , and p were measured directly from the angular accelerometers and the roll gyro, respectively,

and required no corrections. The variations of \dot{q} and \dot{r} were obtained by integration of \ddot{q} and \ddot{r} over several cycles and by assuming that they varied symmetrically about zero values. The angular acceleration in roll \ddot{p} was obtained by differentiating \dot{p} with time.

The values of $a_{L,Lo}$ and $a_{N,n}$ were used for determining $a_{L,cg}$ and $a_{N,cg}$, respectively, throughout most of the flight. The values of $a_{L,Hi}$ were used only at the higher Mach numbers where the deceleration was greater than the range of $a_{L,Lo}$; and $a_{N,t}$ served only as a check for $a_{N,cg}$.

The total force coefficients were determined from the instantaneous values of the translatory accelerations (referenced to the center of gravity) as follows:

$$C_N = \frac{W}{q_\infty S} a_{N,cg} \quad (4)$$

$$-C_X = \frac{W}{q_\infty S} a_{L,cg} \quad (5)$$

and

$$C_Y = \frac{W}{q_\infty S} a_{Y,cg} \quad (6)$$

The total moment coefficients for the rocket model were computed from the instantaneous values of angular acceleration and velocity by using the following expressions:

$$C_m = \frac{I_Y}{q_\infty S \bar{c}} \dot{q} + \left(\frac{I_X - I_Z}{q_\infty S \bar{c}} \right) p r \quad (7)$$

$$C_n = \frac{I_Z}{q_\infty S b} \dot{r} + \left(\frac{I_Y - I_X}{q_\infty S b} \right) p q \quad (8)$$

and

$$C_l = \frac{I_X}{q_\infty S b} \dot{p} + \left(\frac{I_Z - I_Y}{q_\infty S b} \right) q r \quad (9)$$

Analog Simulation

An analog simulation analysis similar to that of references 1 and 3 was used to study rolling velocities of the model near Mach numbers 4 and 2. There were three reasons for using the analog computer for motion simulation: (1) the vehicle aerodynamics were known to be nonlinear with angle of attack or yaw; (2) the lateral and longitudinal aerodynamics were coupled by the rolling velocity; and, (3) the vehicle motions were not symmetrical. The equation associated with the drag force was omitted since the velocity of the model was nearly constant through the time intervals studied. The cross-product inertia terms have been omitted from the equations because the principal axes coincided with the body axes. The equations of motion were written for the body-axis system and are as follows:

Normal force:

$$\dot{\alpha} = q - \beta p - \frac{q_{\infty} S}{mV} C_{L\alpha} \alpha \quad (10)$$

Side force:

$$\dot{\beta} = -r + \alpha p + \frac{q_{\infty} S}{mV} C_{Y\beta} \beta \quad (11)$$

Rolling moment:

$$\dot{p} = \left(\frac{I_Y - I_Z}{I_X} \right) qr + \frac{q_{\infty} S b}{I_X} (C_{l\beta} \beta + C_{l\beta\alpha} \beta \alpha) + \frac{q_{\infty} S b^2}{2VI_X} (C_{lp} p + C_{lr} r) \quad (12)$$

Pitching moment:

$$\dot{q} = \left(\frac{I_Z - I_X}{I_Y} \right) pr + \frac{q_{\infty} S \bar{c}}{I_Y} C_{m\alpha} \alpha + \frac{q_{\infty} S \bar{c}^2}{2VI_Y} (C_{mq} q + C_{m\dot{\alpha}} \dot{\alpha}) \quad (13)$$

Yawing moment:

$$\dot{r} = \left(\frac{I_X - I_Y}{I_Z} \right) pq + \frac{q_{\infty} S b}{I_Z} C_{n\beta} \beta + \frac{q_{\infty} S b^2}{2VI_Z} (C_{nr} r + C_{n\dot{\beta}} \dot{\beta} + C_{np} p) \quad (14)$$

The body was assumed rigid and the gravity terms were omitted from the equations. Certain aerodynamic terms, such as $C_{m\beta}$ and C_{Yr} , were omitted from equations (10) to (14), inasmuch as their effect on the motions was considered to be negligible. In the analog study it was assumed that $\dot{\beta} = -r$ in equation (14), thus allowing some simplification in the last term.

The equations of motion for five degrees of freedom were used at $M = 4$ and $M = 2$. The static stability derivatives from reference 5 were used in the analog study at $M = 2$ after they were transferred from the reference point of reference 5 (66.6 percent of the theoretical body length behind the theoretical apex) to the center of gravity of the vehicle. The damping-in-pitch coefficients C_{mq}

and $C_{m\dot{\alpha}}$ were initially calculated from linearized theory (refs. 6 and 7), but their values were lowered when they were found to be excessive for an accurate simulation of the motions.

The damping-in-yaw coefficients C_{n_r} and $C_{n\dot{\beta}}$ were also calculated in a manner similar to that for pitch, with the assumption that all damping was due to the wing-tip fins and vertical tail. The value for C_{l_p} was estimated from reference 8, and values for C_{l_r} and C_{n_p} were estimated from lifting-line theory. Table III presents values for all the derivatives used. It should be noted that two slopes were used to approximate $C_{Y\beta}$, $C_{n\beta}$, and $C_{l\beta\alpha}$ because they were non-linear with β and/or α . (These slopes were obtained from wind-tunnel tests of ref. 5.) The initial conditions for the equations of motion were obtained at a given time in the free-flight record. Initial values of α and β were found by solving the equations of motion. The initial conditions for the analog investigations made for $M = 4$ and $M = 2$ are given in table IV.

Because of the large predominating effect of $C_{l\beta\alpha}$ on the motions, a highly simplified motion study was made with the use of the following three-degree-of-freedom equations of motion:

$$\dot{\alpha} = -\beta p \quad (15)$$

$$\dot{\beta} = \alpha p \quad (16)$$

$$\dot{p} = \frac{q_{\infty} S b}{I_X} C_{l\beta\alpha} \beta \alpha \quad (17)$$

An analytical solution for this simplified set of equations is included in the appendix.

RESULTS AND DISCUSSION

Basic Data

One of the purposes of the flight test presented in this paper was to determine if the roll rates and accelerations of the basic vehicle could be decreased by the addition of two wing-tip fins. Reference 5 presents longitudinal and lateral stability data for the model of reference 1 (the basic model) at Mach numbers of 1.41 and 2.01 and for the model of this report at a Mach number of 2.01. The Reynolds numbers of these wind-tunnel tests are given in figure 7. As shown in reference 5, the vehicle with wing-tip fins was statically stable at a Mach number of 2.01. As a result of adding wing-tip fins to the basic configuration, wind-tunnel data (ref. 4) at $M = 2.01$ and $\alpha = 4^\circ$ show that $C_{n\beta}$ was increased from 0.0005 to 0.0022 per degree, $C_{l\beta\alpha}$ was decreased from -0.0012 to -0.0014,

$C_{Y\beta}$ was decreased from -0.0020 to -0.0045, and C_m was decreased from 0.0025 to -0.0010, all of which were referenced to the 66.6 percent longitudinal station behind the theoretical apex and/or the wing mean aerodynamic chord. Even though the directional and longitudinal stability was increased, a comparison of the roll-rate histories for the present test and those of reference 1 shows similar types of oscillations for both models. The reason for this result is that the addition of the wing-tip fins did not result in a decrease in $C_{l\beta\alpha}$.

Figure 8(a) shows the time interval from 23.5 to 24.5 seconds, which begins just after model separation (23.48 seconds) and includes the period during which the first pulse-rocket ignition occurred (23.52 seconds). This figure indicates that the model experienced oscillations of large amplitude, due to the pulse rocket, which were coupled in pitch and yaw. The roll rate oscillated about zero through large amplitudes during and immediately after pulse-rocket ignition and then steadily increased to a large positive amplitude of approximately 35 radians per second. The second pulse rocket was ignited at 27.01 seconds. Figure 8(b) presents data from 28.5 to 29.5 seconds and shows the sinusoidal oscillation of the model in roll, pitch, and yaw. Figure 8(c) presents data from 38.6 to 39.6 seconds for $M = 2$ after ignition of the second pulse rocket. In general, the motions of the model were coupled, and the roll rate over some intervals was unsteady and varied randomly from positive roll oscillations through roll reversals.

Vehicle oscillation about the stability boundary was considered as a possible cause of the coupled motions. By using the methods of references 4 and 9, it is possible to superimpose a region of roll divergence for steady roll rates on the curve of figure 9. The figure indicates that from $M = 4.2$ to $M = 3.7$ the roll rates are not in the regions of divergence; however, at lower Mach numbers the roll rates cross back and forth over the boundaries of divergence. It should be noted that the moments are coupled prior to encountering the regions of divergence, which indicates that the cause of the coupling is purely aerodynamic. It should also be noted that the boundaries were derived for constant roll rates and linear equations of motion, which do not account for the second-order effects such as that of $C_{l\beta\alpha}$, and, consequently, the boundaries may not be applicable for this flight condition.

The variation of the total force and moment coefficients with time is presented in figures 10 to 13 for four time increments. The time increments were picked to show variation in aerodynamics (1) after model separation and during first pulse-rocket ignition at $M \approx 4.1$; (2) after first pulse-rocket disturbance at $M \approx 3.9$; (3) after second pulse-rocket disturbance at $M = 3.1$; and (4) after second pulse-rocket disturbance at $M \approx 2.1$. Parts (a) and (b) of these figures are the longitudinal coefficients, total normal force and total pitching moment, respectively. Parts (e) and (f) are the directional coefficients, total side force and total yawing moment, respectively; parts (c) and (g) are total axial force and total rolling-moment coefficients, respectively. Parts (d) and (h) of figures 10 to 13 are variations of total pitching moment plotted against total normal-force coefficient and of total yawing moment plotted against total side-force coefficient, respectively. A line representing the approximate slope of the data has been drawn through some of the curves indicating static stability as shown by

reference 5 but these curves do not pass through zero (at $C_N = 0$ and $C_Y = 0$), probably because of the asymmetries due to model construction, as well as the effects of the cross-coupling moments and forces. The model also appears to exhibit a trim change with Mach number.

In figure 10(c) the reduction in axial force is evident and is due to afterburning in the separation motor from about 23.62 to 23.90 seconds. The variation in base pressure shown in figure 8(a) is also due to the effects of afterburning.

Analog Analysis

Five-degree-of-freedom analog analysis.— The first attempt at analyzing the flight data herein was to compare the longitudinal and lateral aerodynamic coefficients and derivatives obtained by simple analysis with those presented in references 1 and 5. However, the coupled forces and moments did not allow sufficient steady-state motion for comparison.

Numerous analog runs were made using the five-degree-of-freedom equations at $M = 4$ and $M = 2$. In an effort to make adjustments to the coefficients for proper motion simulation, it was found that $C_{l\beta\alpha}$ was predominant in its effect on the rolling motion. By the use of the aerodynamic coefficients of table III and the initial conditions of table IV, figures 14 and 15 were selected as representative of the flight rolling velocity at $M = 4$ and $M = 2$, respectively. Figures 16 and 17 are reproductions from the flight record of the rolling velocity and pitch and yaw accelerations for $M = 4$ and $M = 2$, respectively.

Comparison of figures 14 and 16 indicates that a qualitative type of agreement is obtained between the analog record and the flight record. Comparison of figures 15 and 17 indicates the same type of agreement, but in this case there appears to be closer quantitative agreement.

Three-degree-of-freedom analog analysis.— The manner in which $C_{l\beta\alpha}$ seemed to dominate the five-degree-of-freedom analog studies indicated that a greatly simplified approach to the simulation of the rolling velocities was possible. Equations (15), (16), and (17) were used for the simplified three-degree-of-freedom analysis. Analog studies were made of the rolling velocities at $M = 4$ (fig. 18) and at $M = 2$ (fig. 19). Comparison of figures 18 and 14 shows the effect of the simplified analysis. In figure 18 the frequency and amplitude of the rolling-velocity oscillation is more obvious than in figure 14 and agrees better with the periodic rolling velocity shown in the flight data at $M = 4$ (fig. 16). Figure 19 is an analog record of the rolling velocity at $M = 2$ and shows, in the initial moments of the run, a roll-reversal motion similar to those of the flight record followed by a negative periodic rolling velocity. Figure 19 was selected as being typical of the analog runs made at $M = 2$ with the simplified equations of motion.

Consecutive analog runs showed that the simulated motions would not repeat exactly for identical initial conditions. The angular velocities and their frequencies were similar to those from the test. Small variations in the stability

derivatives and use of other sets of initial conditions did not provide repeatability. The nonrepeatability appeared to be due to the sensitivity of the equations to small computer errors of the analog for the inputs used. These small computer errors may be compared to spurious disturbances during the flight and, in this case, are partly responsible for the realistic simulation of the free-flight motions. The analytical solution to the equations of motion given in the appendix shows that the type of rolling motion experienced depends on a parameter k which in turn depends on the initial conditions, dynamic pressure, and the $C_{l\beta\alpha}$ derivative. For values of $k < 1$, the solution gives rise to a periodic positive or negative rolling velocity, whereas, for values of $k > 1$, oscillatory rolling velocities (roll reversals) are predicted. A value of $k = 1$ yields a logarithmic decay to zero of rolling velocity, but it is a very sensitive condition and not likely to show itself in flight.

Several calculations have been made using the analytical expressions of the appendix to make comparisons with flight rolling-velocity time histories. The rolling-velocity time histories for $k < 1$, $k = 1$, and $k > 1$ were computed for the comparisons. The value of k for the case in which $k < 1$ was determined from equation (A23) of the appendix for which the flight values of p_{max} and p_{min} were used; hence, in this instance, the three-degree-of-freedom equations of motion may be judged only by the agreement of the general shapes of the flight and computed curves and the period of the motions. Figure 20 ($k = 0.80$) shows that the simplified three-degree-of-freedom equations predicted both the period and general shape of the rolling-velocity variations very well and also indicates, at least for the portion of the flight shown in figure 20, that the q and r velocities did not appreciably affect the rolling motion.

Calculations of k for $k = 1.004$ were made with the expression for the period of oscillation given as equation (A21) in the appendix. Figure 21 shows that the amplitudes are fairly well predicted by the three-degree-of-freedom equations of motion; however, the shapes of the two curves do not agree as well as for the case when $k = 0.80$.

A portion of the flight record which has a value of k of approximately 1.0 has been selected for comparison with the theoretical prediction in figure 22. For the actual theoretical case, the half-cycle logarithmic decay of roll rate to zero occurs at infinity. For practical purposes, two half-cycles which decay logarithmically to zero and which have a half-period equal to flight-record half-period obtained for $k = 1.0$ from the three-degree-of-freedom equations of motion are compared with the flight record. Figure 22 shows that the comparison can be considered comparable in only a qualitative manner. The differences between the theoretical curve and experimental values may be due largely to the fact that the simplified theory neglects the effects of q and r . Better agreement is indicated in figure 15 where the rolling-velocity time histories have been determined from the equations of motion for five degrees of freedom and for values of k of approximately 1.0.

It should be noted that for similar highly swept low-aspect-ratio glider configurations with and without planar symmetry, as described in the wind-tunnel tests of reference 5, $C_{l\beta\alpha}$ is approximately the same magnitude. According to

the general analog study made herein, the aforementioned configurations would be subject to similar coupled motions as obtained from the present flight test at supersonic speeds unless provision is made for roll or yaw control.

CONCLUDING REMARKS

Results from a free-flight investigation conducted to determine the aerodynamic characteristics and motions of a simplified hypersonic glider configuration, which had planar symmetry and the mass concentrated along the longitudinal axis, indicated that the flight motions were coupled and nonlinear and that the model experienced unsteady rolling velocities up to 35 radians per second. The directional and longitudinal stability was increased by the addition of wing-tip fins, as shown by wind-tunnel tests. The coupled rolling motions of the model were similar to those of the same model without the wing-tip fins. The model was statically and dynamically stable in pitch and yaw at small angles of attack and sideslip up to a Mach number of 4.

Electronic analog studies using equations of motion for five degrees of freedom of the rolling velocities of the model indicated that the rate of change of the effective-dihedral derivative with change in angle of attack $C_{l_{\beta\alpha}}$ was the predominant term in the simulation of the amplitude and period of the rolling motions. An analytical solution of the simplified three-degree-of-freedom equations of motion containing the $C_{l_{\beta\alpha}}$ derivative yielded a critical roll-rate parameter which correlated the type of rolling motions experienced by the configuration.

The analog study showed that the term $C_{l_{\beta\alpha}}$ was a significant cross-coupling derivative for the configuration studied and should be considered for predicting the flight motions of configurations which are highly swept and have their mass concentrated along the longitudinal axis.

Langley Research Center,
National Aeronautics and Space Administration,
Langley Station, Hampton, Va., July 30, 1963.

APPENDIX

AN ANALYTICAL SOLUTION OF THE SIMPLIFIED THREE-DEGREE-OF-FREEDOM EQUATIONS OF MOTION

By Percy J. Bobbitt

The simplified three-degree-of-freedom equations

$$\dot{\alpha} = -\beta p = -\beta \dot{\phi} \quad (A1)$$

$$\dot{\beta} = \alpha p = \alpha \dot{\phi} \quad (A2)$$

and

$$\dot{p} = \frac{q_{\infty} S b}{I_X} C_{l_{\beta\alpha}} \beta \alpha = \ddot{\phi} \quad (A3)$$

(eqs. (15), (16), and (17), respectively, of the text) which yield motions similar in several respects to the flight records and five-degree-of-freedom equations are easily integrated and have their parallel in dynamics in the pendulum problem. Of primary interest here is this isolation of the critical parameter which determines the characteristics of the motion.

It is a slight convenience in effecting a solution of the equations of motion to normalize α and β by $\sigma_0 = \sqrt{\alpha_0^2 + \beta_0^2}$, so that equations (A1) to (A3) become

$$\dot{\bar{\alpha}} = -\bar{\beta} p \quad (A4)$$

$$\dot{\bar{\beta}} = \bar{\alpha} p \quad (A5)$$

and

$$\dot{p} = -C_0 \bar{\beta} \bar{\alpha} \quad (A6)$$

where

$$C_0 = - \frac{q_{\infty} S b}{I_X} C_{l_{\beta\alpha}} \sigma_0^2 \quad (A7)$$

$$\bar{\beta} = \frac{\beta}{\sqrt{\alpha_0^2 + \beta_0^2}}$$

and

$$\bar{\alpha} = \frac{\alpha}{\sqrt{\alpha_o^2 + \beta_o^2}}$$

If $\bar{\alpha}$ is eliminated from equations (A5) and (A6), the following differential equation is obtained:

$$p\dot{p} = -C_o\bar{\beta}\dot{\bar{\beta}} \quad (A8)$$

Integrating equation (A8) and subsequently solving for p yields

$$p = \pm \sqrt{p_o^2 + C_o\bar{\beta}_o^2} \sqrt{1 - \left(\frac{C_o}{p_o^2 + C_o\bar{\beta}_o^2} \right) \bar{\beta}^2} \quad (A9)$$

A similar equation in terms of $\bar{\alpha}$ may be derived by eliminating $\bar{\beta}$ from equations (A4) and (A6) and integrating.

If the equation resulting from the division of equation (A4) by equation (A5) is integrated, the relation between $\bar{\alpha}$ and $\bar{\beta}$ is given by

$$\bar{\alpha}^2 + \bar{\beta}^2 = \bar{\alpha}_o^2 + \bar{\beta}_o^2 = 1 \quad (A10)$$

and it becomes clear that $\bar{\alpha}$ and $\bar{\beta}$ may be set equal to $\sin \phi$ and $-\cos \phi$, respectively, or $\cos \phi$ and $\sin \phi$, respectively. Choosing

$$\bar{\alpha} = \cos \phi \quad (A11)$$

and

$$\bar{\beta} = \sin \phi \quad (A12)$$

the equation for p (eq. (A9)) may now be written

$$p = \dot{\phi} = \pm \frac{\sqrt{C_o}}{k} \sqrt{1 - k^2 \sin^2 \phi} \quad (A13)$$

or

$$\pm \frac{k}{\sqrt{C_o}} \int_{\phi_o}^{\phi} \frac{d\phi}{\sqrt{1 - k^2 \sin^2 \phi}} = \int_0^t dt \quad (A13a)$$

where

$$k = \frac{\sqrt{C_o}}{\sqrt{p_o^2 + C_o\bar{\beta}_o^2}} \quad (A14)$$

The integration of equation (A13) takes three different forms, depending on whether k is less than, greater than, or equal to 1.0. The expressions for t are as follows:

For $k < 1.0$,

$$t = \pm \frac{k}{\sqrt{C_0}} [F(\phi, k) - F(\phi_0, k)] \quad (A15)$$

For $k > 1.0$,

$$t = \pm \frac{1}{\sqrt{C_0}} [F(\psi, 1/k) - F(\psi_0, 1/k)] \quad (A16)$$

where

$$\psi = \sin^{-1}(k \sin \phi)$$

and

$$k \sin \phi \leq 1$$

And, for $k = 1$,

$$t = \pm \frac{1}{2\sqrt{C_0}} \log_e \left(\frac{1 + \sin \phi}{1 - \sin \phi} - \log_e \frac{1 + \sin \phi_0}{1 - \sin \phi_0} \right) \quad (A17)$$

where the plus sign denotes positive values of ϕ , and the minus sign denotes negative values of ϕ . (Note that $F(-\phi, k) = F(\phi, k)$.) When ϕ in equation (A15) becomes greater than 90° , the extension-of-range formulas for the elliptic function F must be used; that is, for $\pi/2 \leq \phi \leq \pi$,

$$F(\phi, k) = 2F(\pi/2, k) - F(\pi - \phi, k) \quad (A18a)$$

for $\pi \leq \phi \leq \frac{3\pi}{2}$,

$$F(\phi, k) = 2F(\pi/2, k) + F(\phi - \pi, k) \quad (A18b)$$

and for $\frac{3\pi}{2} \leq \phi \leq \pi$,

$$F(\phi, k) = 4F(\pi/2, k) - F(2\pi - \phi, k) \quad (A18c)$$

For equation (A16), ψ becomes equal to but does not exceed 90° (hence, ϕ will not exceed $\sin^{-1} \frac{\sin \psi}{k}$), and ϕ will reverse its sign when ψ reaches 90° ; this condition is consistent with the fact that ϕ is an even function of ψ about $\psi = 90^\circ$. The equations for time in this case must take a different form.

For

$$t > \pm \frac{1}{\sqrt{C_0}} \left[F(\pi/2, 1/k) - F(\psi_0, 1/k) \right] \quad (A19a)$$

$F(\psi, k)$ is replaced by $2F(\pi/2, 1/k) - F(\psi, 1/k)$; for

$$t > \pm \frac{1}{\sqrt{C_0}} \left[2F(\pi/2, 1/k) - F(\psi_0, 1/k) \right] \quad (A19b)$$

$F(\psi, k)$ is replaced by $2F(\pi/2, 1/k) - F(\psi, 1/k)$; for

$$t > \pm \frac{1}{\sqrt{C_0}} \left[3F(\pi/2, 1/k) - F(\psi_0, 1/k) \right] \quad (A19c)$$

$F(\psi, k)$ is replaced by $4F(\pi/2, 1/k) + F(\psi, 1/k)$.

From equations (A15) and (A16), the revolutions per second in the case of $k < 1$ and the oscillations per second in the case of $k > 1$ are seen to be

$$\frac{\text{Revolutions}}{\text{Second}} = \frac{\sqrt{C_0}}{4kK(k)} \quad (k < 1) \quad (A20)$$

and

$$\frac{\text{Oscillations}}{\text{Second}} = \frac{\sqrt{C_0}}{4K(1/k)} \quad (k > 1) \quad (A21)$$

For $k = 1.0$, p decays logarithmically to zero as ϕ goes to 90° .

In comparing flight roll-rate data with those computed from equations (A13) to (A17), it is necessary to determine an appropriate value of k . It is possible to compute k directly from equation (A14) if a number of points along a cycle are averaged, since

$$k = \frac{\sqrt{C_0}}{\sqrt{p_0^2 + C_0 \bar{\beta}_0^2}} = \frac{\sqrt{C_0}}{\sqrt{p^2 + C_0 \bar{\beta}^2}} \quad (A22)$$

However, better results will usually be obtained if k is computed from the formula for oscillations per second for $k > 1$ (eq. (A21)) or, in the case of $k < 1$, by measuring p_{\max} and p_{\min} and noting that

$$\frac{p_{\min}}{p_{\max}} = \sqrt{1 - k^2} \quad \text{or} \quad k = \sqrt{1 - \left(\frac{p_{\min}}{p_{\max}} \right)^2} \quad (A23)$$

REFERENCES

1. Hoffman, Sherwood, and Blanchard, Willard S., Jr.: Free-Flight Investigation at Supersonic Speeds of the Stability and Drag of a 79° Clipped Delta Boost-Glide Configuration Including an Analog Study of Coupled Motions During the Flight. NASA TM X-425, 1961.
2. Malvestuto, Frank S., Jr., and Margolis, Kenneth: Theoretical Stability Derivatives of Thin Sweptback Wings Tapered to a Point With Sweptback or Sweptforward Trailing Edges for a Limited Range of Supersonic Speeds. NACA Rep. 971, 1950. (Supersedes NACA TN 1761.)
3. Gillis, Clarence L.: A Brief Analog Investigation of Inertia Coupling in Rolling Maneuvers of an Airplane Configuration Using a Variable-Incidence Wing as the Longitudinal Control. NACA RM L57F18, 1957.
4. Sternfield, Leonard: A Simplified Method for Approximating the Transient Motion in Angles of Attack and Sideslip During a Constant Rolling Maneuver. NACA Rep. 1344, 1958. (Supersedes NACA RM L56F04.)
5. Foster, Gerald V.: Static Stability Characteristics of a Series of Hypersonic Boost-Glide Configurations at Mach Numbers of 1.41 and 2.01. NASA TM X-167, 1959.
6. Malvestuto, Frank S., Jr., and Hoover, Dorothy M.: Lift and Pitching Derivatives of Thin Sweptback Tapered Wings With Streamwise Tips and Subsonic Leading Edges at Supersonic Speeds. NACA TN 2294, 1951.
7. Malvestuto, Frank S., Jr., and Hoover, Dorothy M.: Supersonic Lift and Pitching Moment of Thin Sweptback Tapered Wings Produced by Constant Vertical Acceleration - Subsonic Leading Edges and Supersonic Trailing Edges. NACA TN 2315, 1951.
8. Malvestuto, Frank S., Jr., Margolis, Kenneth, and Ribner, Herbert S.: Theoretical Lift and Damping in Roll at Supersonic Speeds of Thin Sweptback Tapered Wings With Streamwise Tips, Subsonic Leading Edges, and Supersonic Trailing Edges. NACA Rep. 970, 1950. (Supersedes NACA TN 1860.)
9. Phillips, William H.: Effect of Steady Rolling on Longitudinal and Directional Stability. NACA TN 1627, 1948.

TABLE I.- PHYSICAL CHARACTERISTICS OF ROCKET MODEL

Wing:

Planform area, sq ft	5.87
Base area, sq ft	0.64
Span, ft	1.77
Aspect ratio	0.53
Root chord (model length to theoretical tip), ft	5.56
Mean aerodynamic chord, ft	3.83
Distance from mean aerodynamic chord to root chord, ft	0.34
Sweepback angle of leading edge, deg	78.87
Dihedral, deg	0.00
Maximum thickness ratio	0.077
Taper ratio	0.191

Vertical tail:

Lateral area (two fins exposed), sq ft	0.36
Base area (two fins exposed), sq ft	0.05
Span (total), ft	0.85
Aspect ratio	2.0
Sweepback angle of leading edge, deg	76.00
Wedge half-angle, deg	3.82
Taper ratio	0.33

Fins:

Lateral area (one fin exposed), sq ft	0.40
Base area (two fins exposed), sq ft	0.10
Span, ft	0.62
Aspect ratio	0.96
Planform area (two fins exposed), sq ft	0.15
Sweepback angle of leading edge, deg	70.00
Taper ratio	0.20
Wedge angle, deg	7.48

Mass characteristics:

Weight, lb	112.73
Center-of-gravity position, rearward from theoretical tip, percent of total body length	54.31
Mass moment of inertia in roll, (slug)(sq ft)	0.38
Mass moment of inertia in pitch, (slugs)(sq ft)	7.86
Mass moment of inertia in yaw, (slugs)(sq ft)	7.99
Product of inertia, (slug)(sq ft)	0.00
Inclination of principal axes to model center line, deg	0.00

TABLE II.- MODEL INSTRUMENT LOCATIONS

Instrument	Quantities measured	Range	Distance from center of gravity ^a		
			x, ft	y, ft	z, ft
Longitudinal accelerometer	$a_{L,Hi}$	1 to -12	-0.375	0.042	0
Longitudinal accelerometer	$a_{L,Lo}$	1 to -2	-.375	-.042	0
Normal accelerometer	$a_{N,n}$	40 to -40	-.175	0	-.067
Normal accelerometer	$a_{N,t}$	30 to -30	2.020	0	-.053
Transverse accelerometer	a_y	30 to -30	-.533	-.033	0
Angular accelerometer in pitch	\dot{q}	300 to -300	.050	-.067	0
Angular accelerometer in yaw	\dot{r}	300 to -300	-.175	0	.067
Angular velocity in roll	p	35 to -35	.300	0	0
			Location		
Total pressure	p_o	0 to 200	Nose tip		
Base pressure	p_b	0 to 15	Manifolded tube on base center line (fig. 3(b))		

^aPositive directions are as shown in figure 1.

TABLE III.- AERODYNAMIC COEFFICIENTS FOR FIVE-DEGREE-OF-FREEDOM
EQUATIONS OF MOTION AT $M = 2$ AND $M = 4$

Coefficient	Mach number	
	$M = 2$	$M = 4$
$C_{L\alpha}$	1.35	0.80
$C_{m\alpha}$	-0.20	-0.05
C_{mq}	-0.01	-0.007
$C_{m\ddot{\alpha}}$	-0.01	-0.003
$C_{l\beta}$	0	0
C_{lp}	-0.08	-0.005
C_{lr}	0.03	0.02
C_{np}	-0.05	-0.05
$C_{nr} - C_{n\dot{\beta}}$	-0.05	-0.01
$C_{Y\beta}$		-0.15
For $0 < \beta < 0.15$	-0.30	
For $0.15 < \beta$	-0.43	
$C_{n\beta}$		-0.20
For $0 < \beta < 0.075$	0.28	
For $0.075 < \beta$	0.32	
$C_{l\beta\alpha}$		-1.64
For $0 < \alpha < 0.1$	-1.10	
For $0.1 < \alpha$	-0.30	

TABLE IV.- INITIAL CONDITIONS FOR FIVE-DEGREE-OF-FREEDOM
EQUATIONS OF MOTION AT $M = 2$ AND $M = 4$

Initial conditions	Mach number	
	$M = 2$	$M = 4$
M	2.148	3.924
V , ft/sec	2,096	3,736
q_{∞} , lb/sq ft	243.7	4,044.8
α , radian	-0.196	-0.039
β , radian	0.160	-0.0022
p , radians/sec	13.5	32.68
q , radians/sec	-1.135	-2.00
r , radian/sec	-0.70	0
\dot{p} , radians/sec ²	240.0	-100.0
\dot{q} , radians/sec ²	37.0	222.2
\dot{r} , radians/sec ²	21.0	47.20
W/qS	0.081	0.0049
p_{∞} , lb/sq in	0.524	2.606
h , ft	74,844	42,207

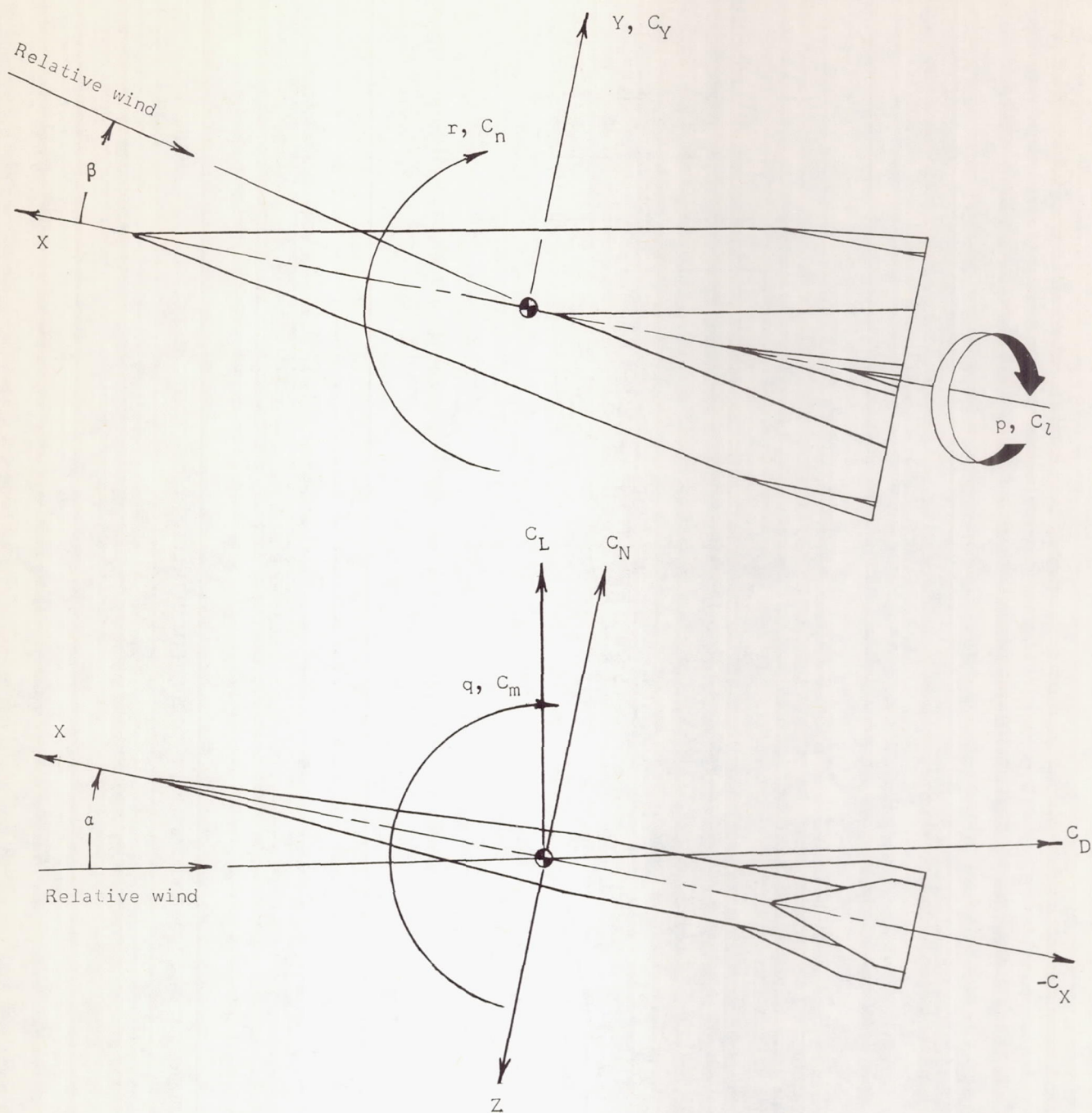


Figure 1.- Body-axis system. Axis origin is at 54.3-percent longitudinal station. (Arrows indicate positive directions.)

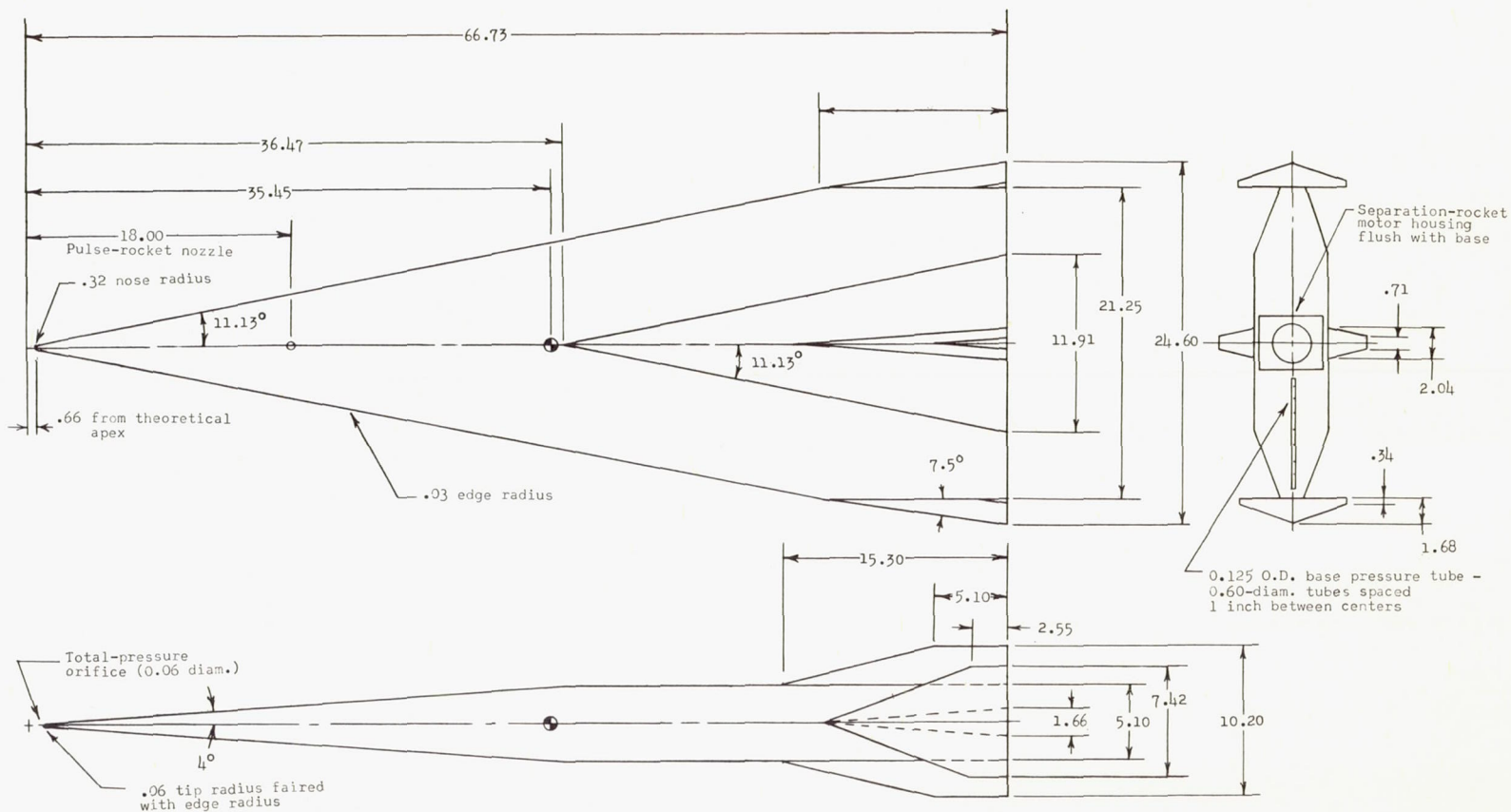
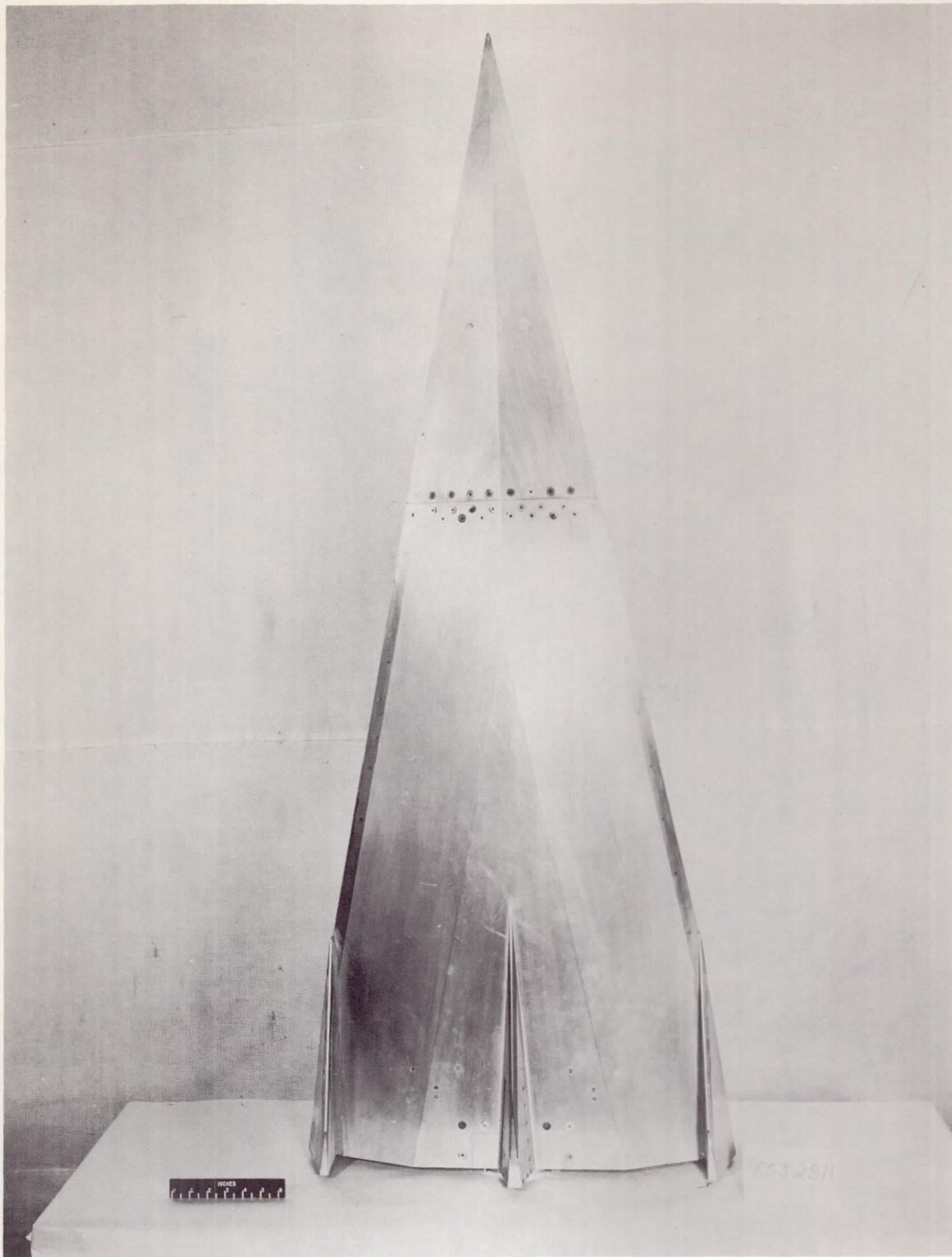


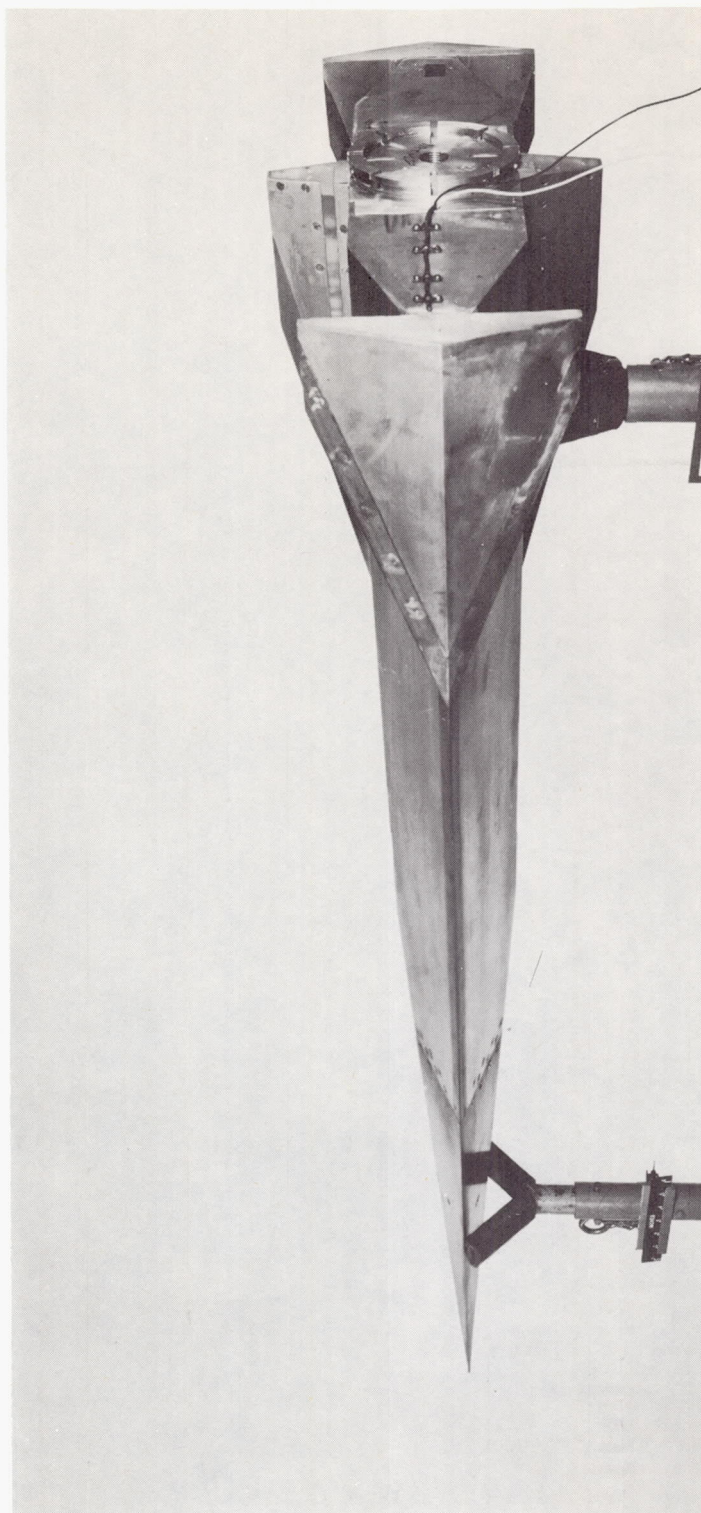
Figure 2.- Details and dimensions of models. (All dimensions are in inches unless otherwise specified.)



(a) Plan view of model.

L-59-3497

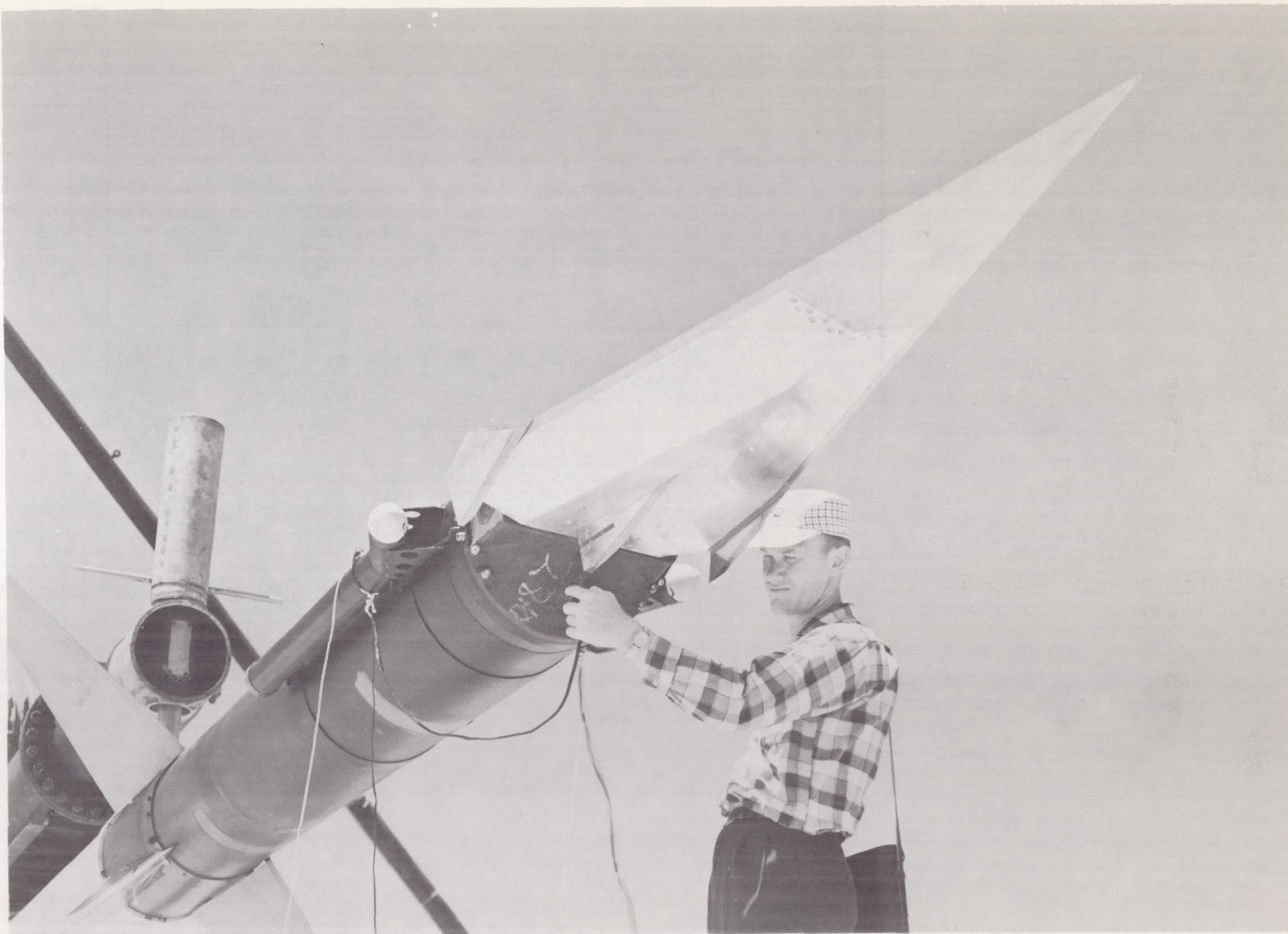
Figure 3.- Free-flight model.



L-59-3495

(b) Three-quarter rear view of model.

Figure 3.- Continued.



(c) Model installed on launch vehicle with retrorockets.

L-59-3809

Figure 3.- Concluded.

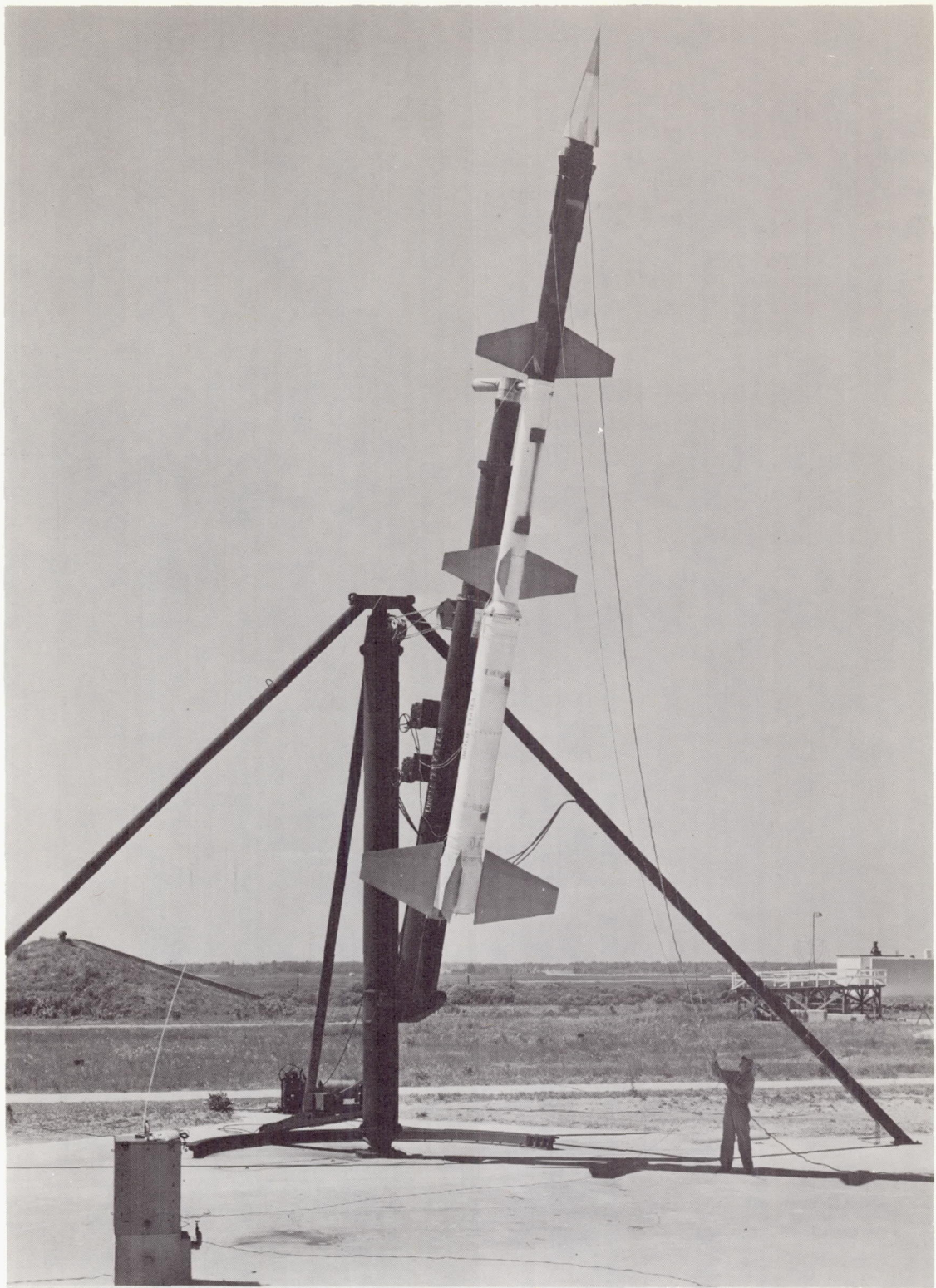


Figure 4.- Model and launch vehicle on launcher.

L-59-3807

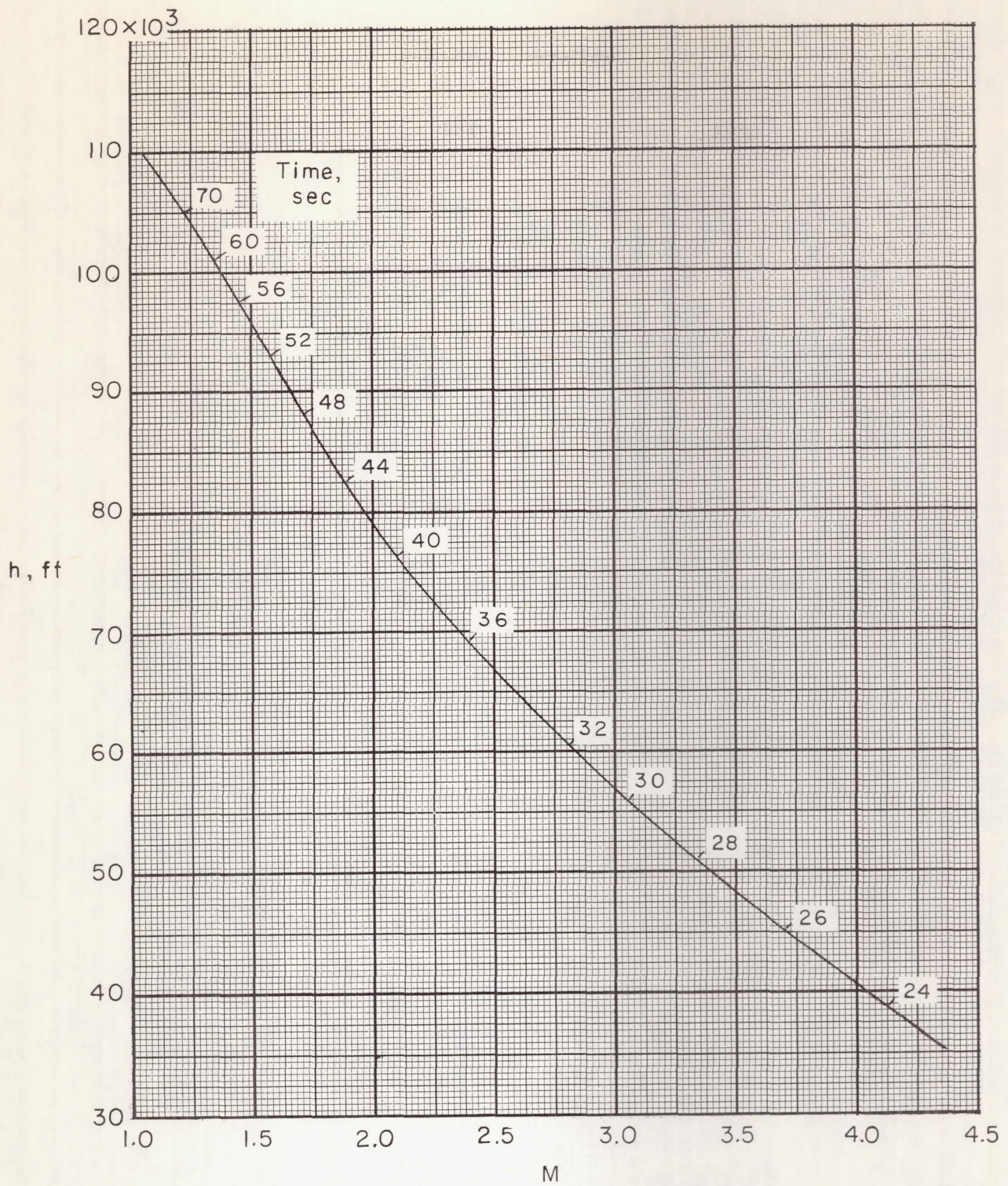


Figure 5.- Time variation of altitude with Mach number.

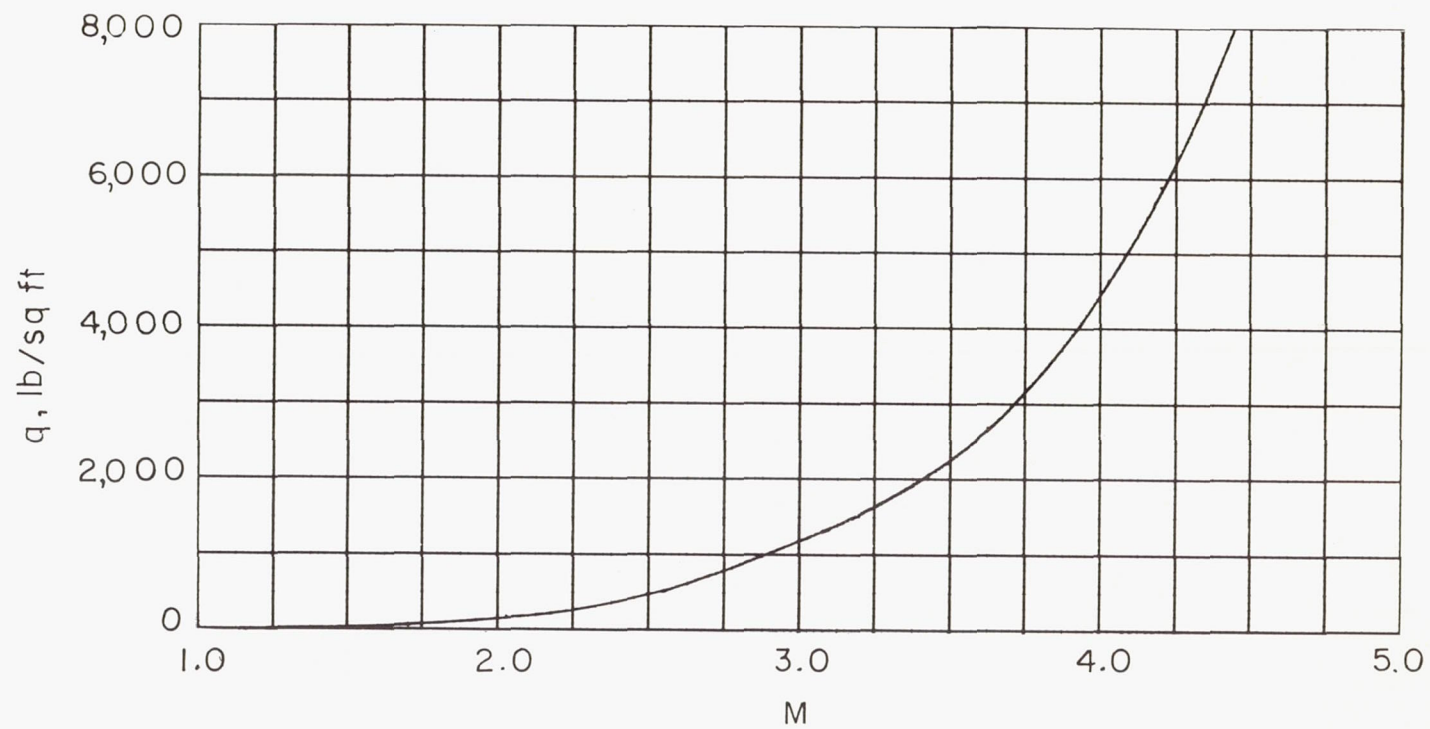


Figure 6.- Variation of free-stream dynamic pressure with Mach number.

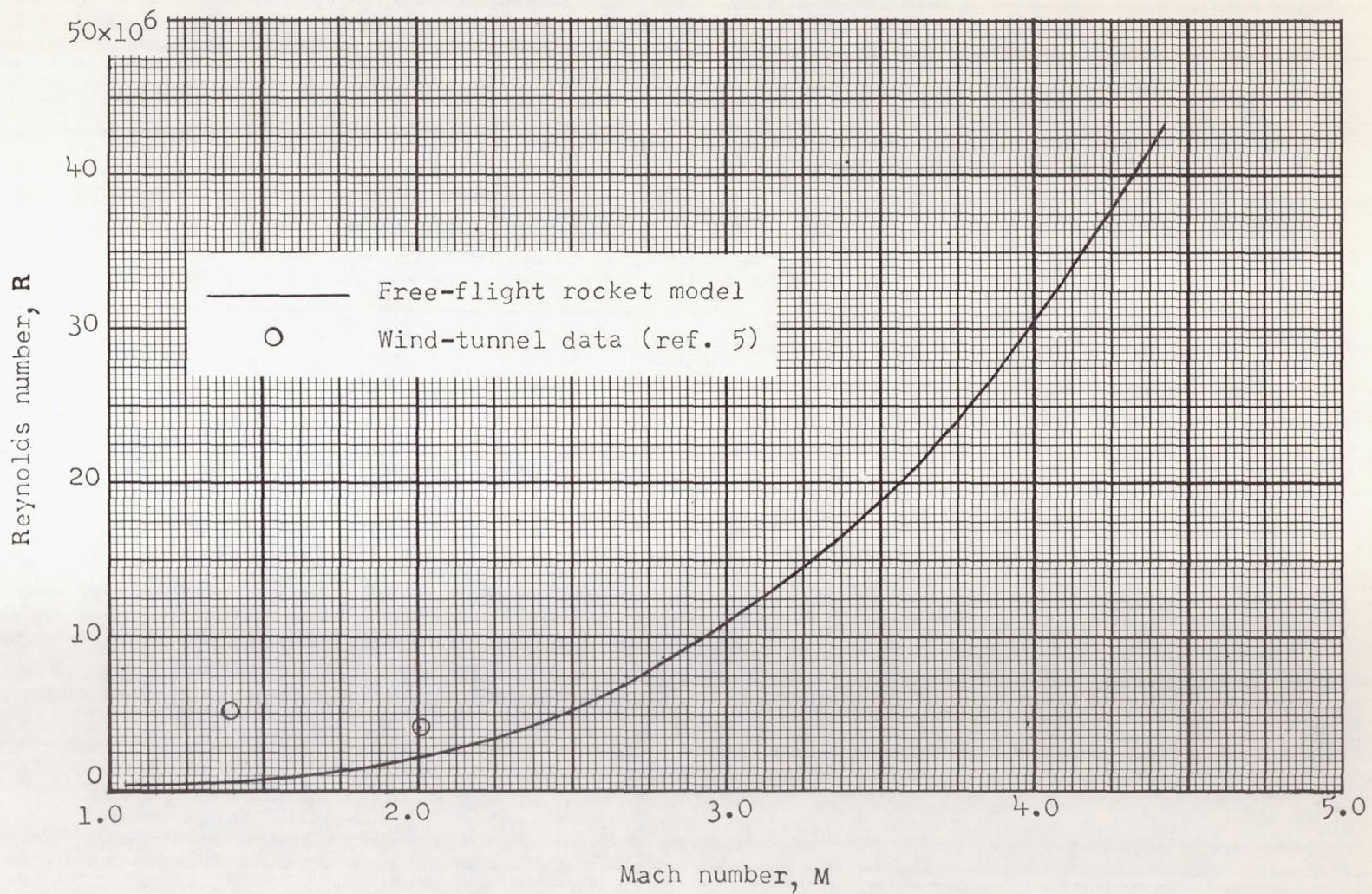
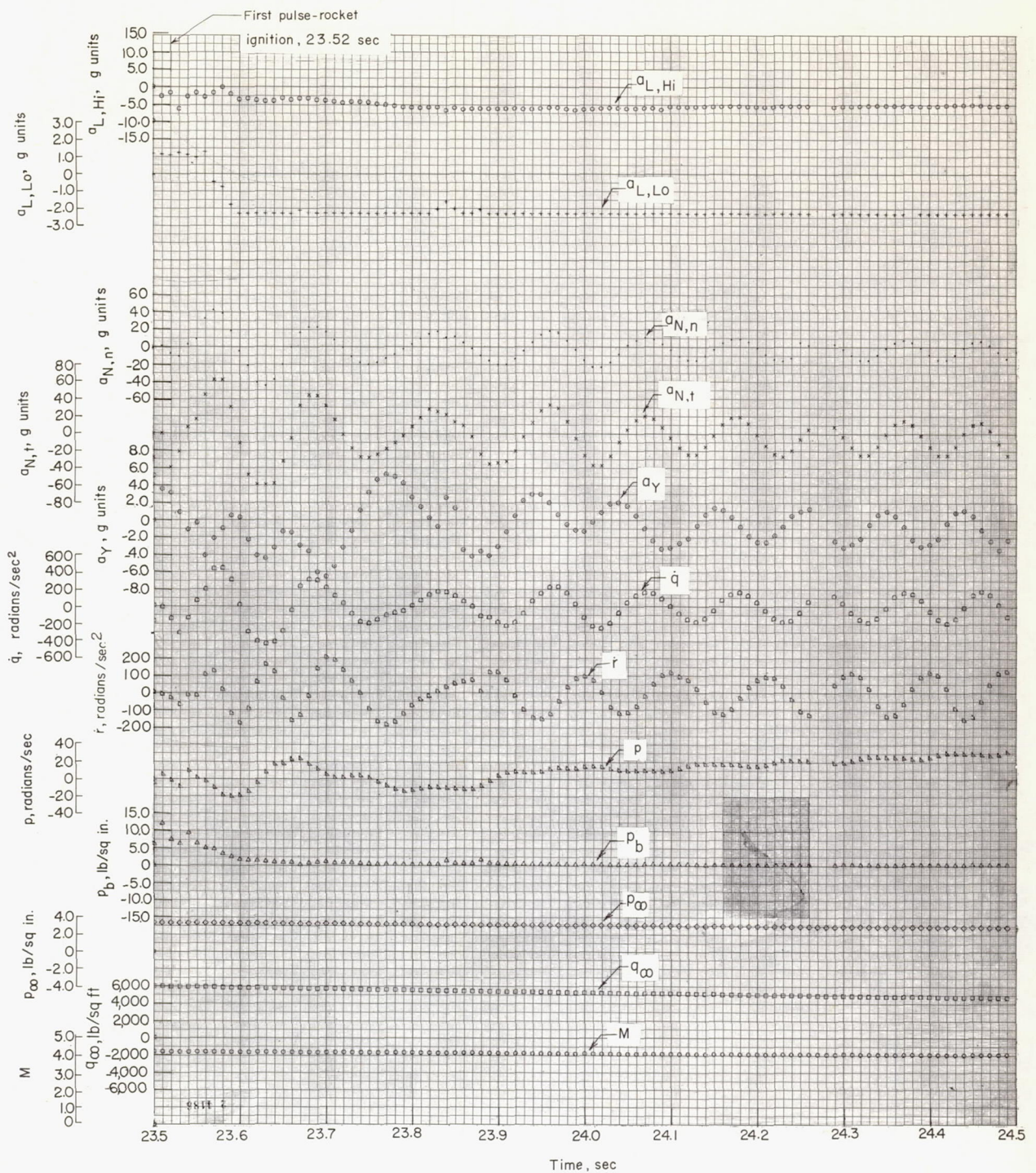
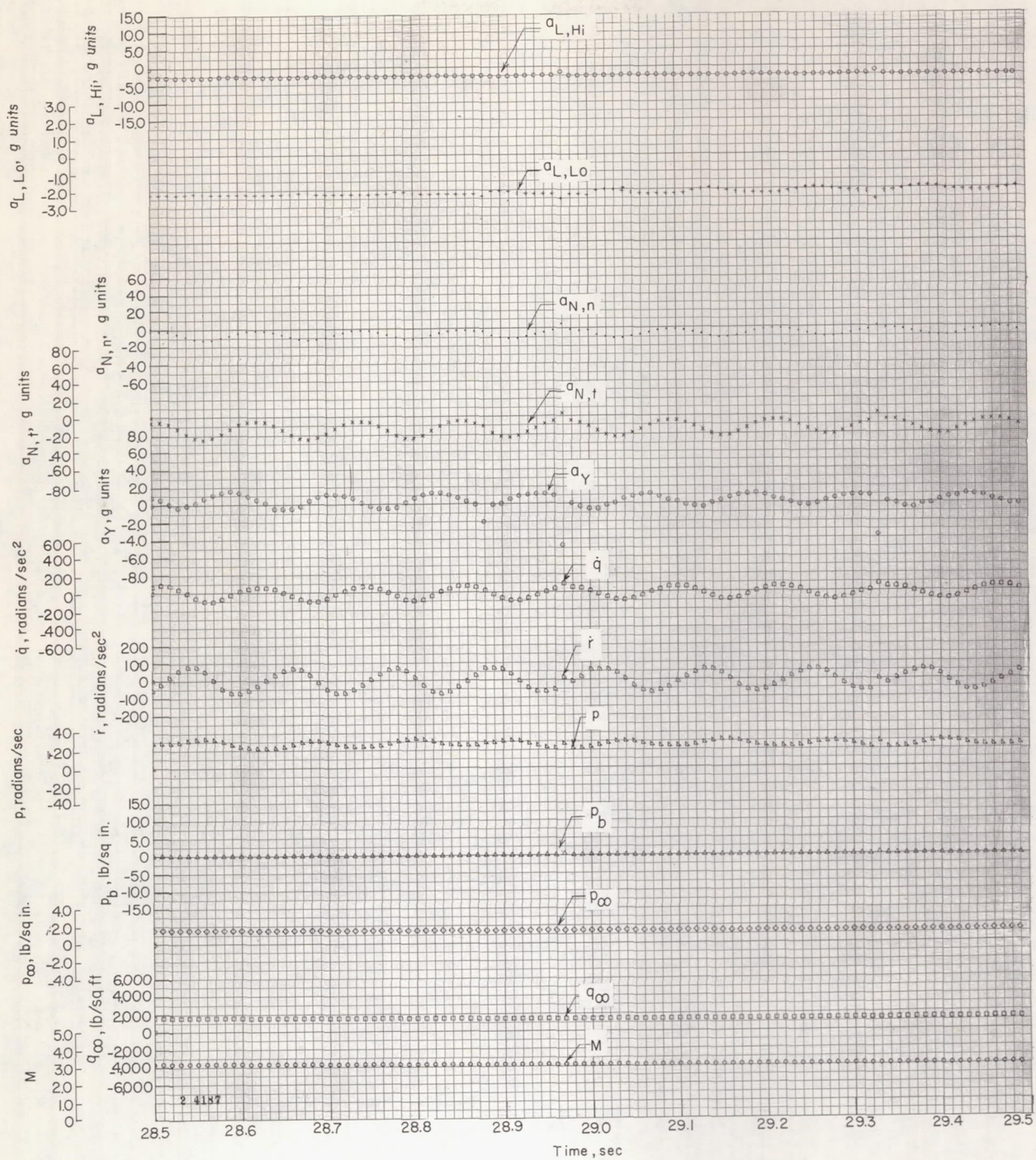


Figure 7.- Variation of Reynolds number, based on mean aerodynamic chord, with Mach number for free-flight rocket model and wind-tunnel tests of reference 5.



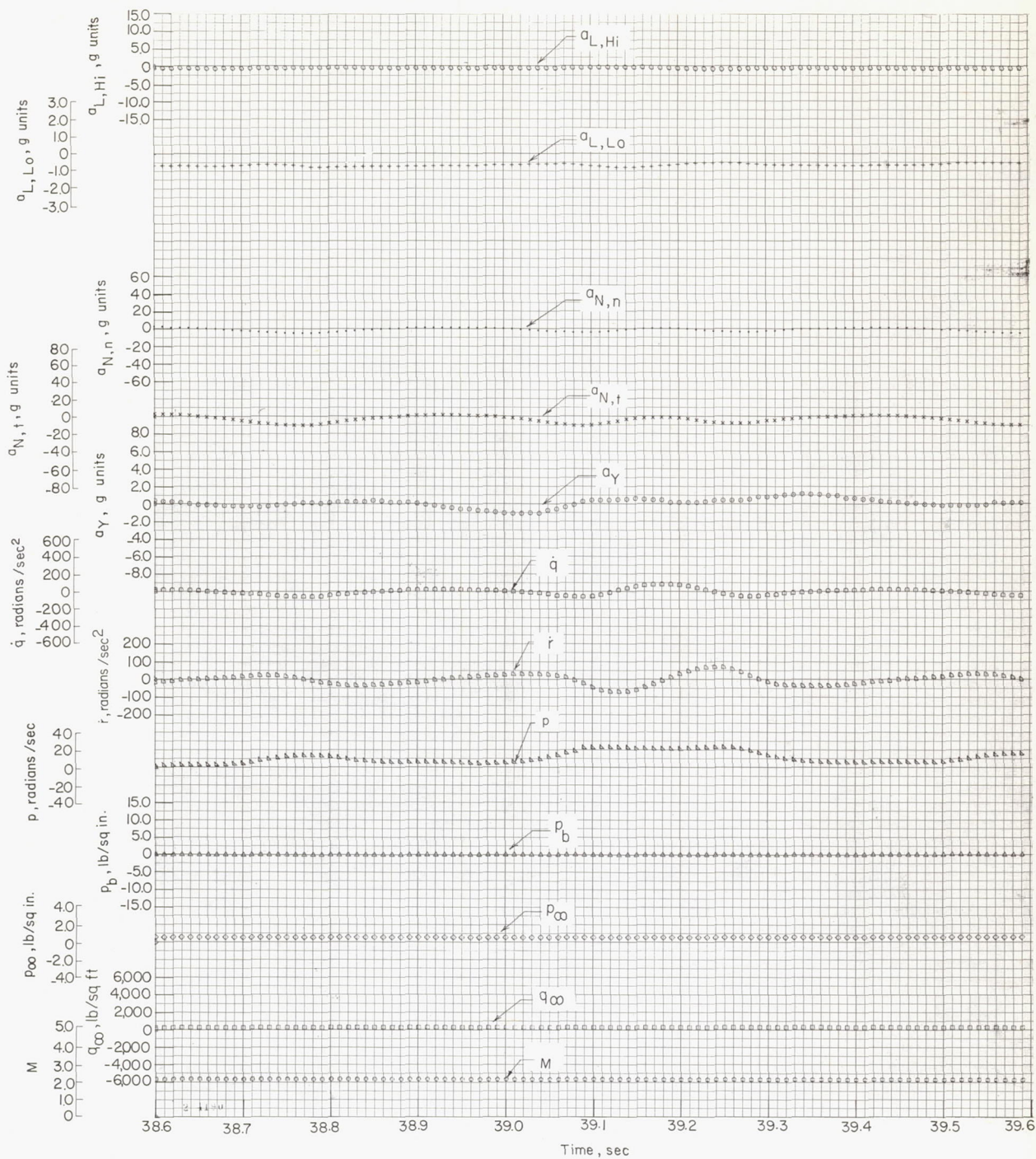
(a) Time interval after model separation (23.48 sec) and before, during, and after first pulse-rocket disturbance.

Figure 8.- Variations of basic data and free-stream conditions with time for three time intervals of flight.



(b) Time interval after second pulse-rocket disturbance. $M = 3.0$.

Figure 8.- Continued.



(c) Time interval after second pulse-rocket disturbance. $M = 2.0$.

Figure 8.- Concluded.

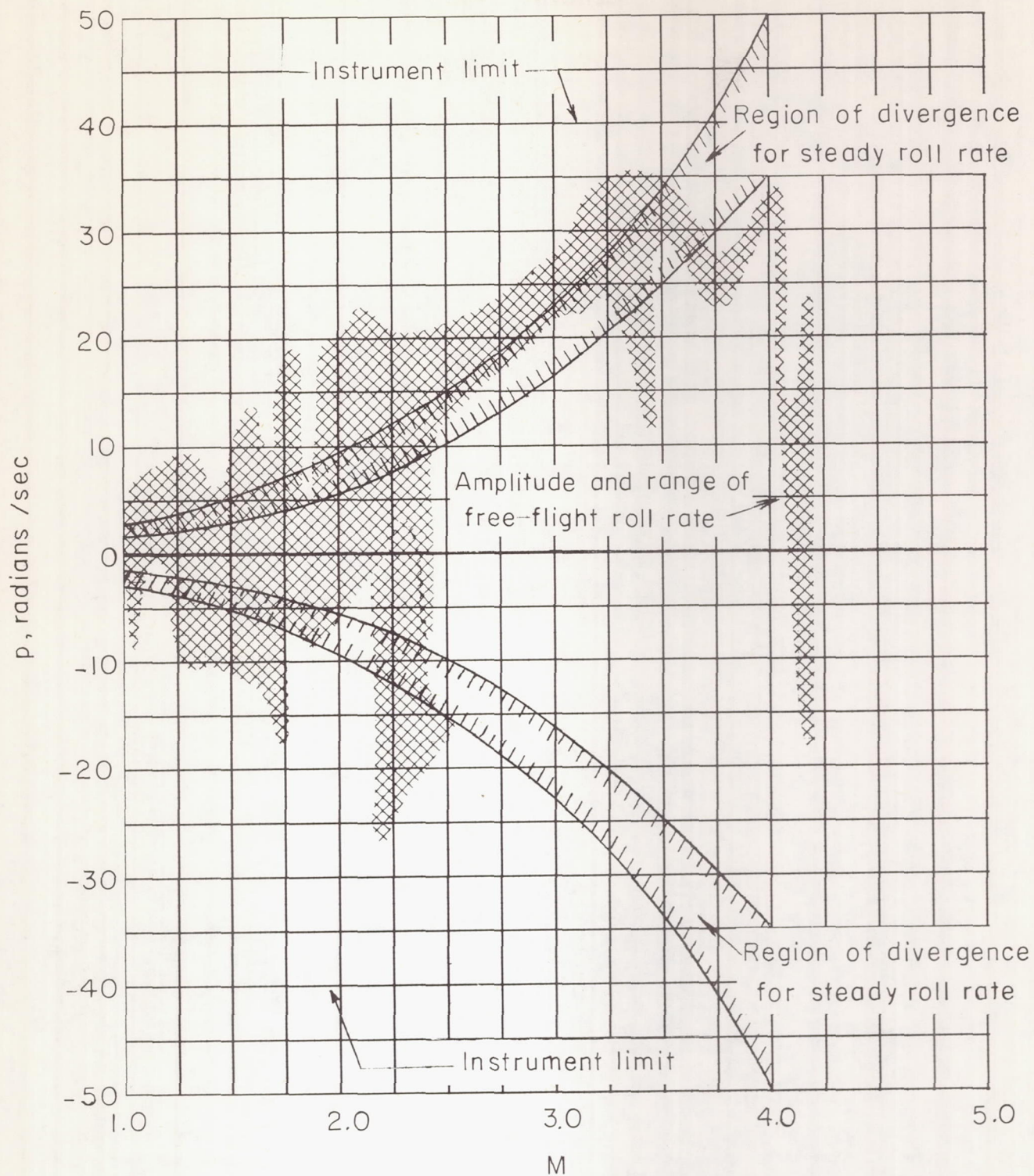
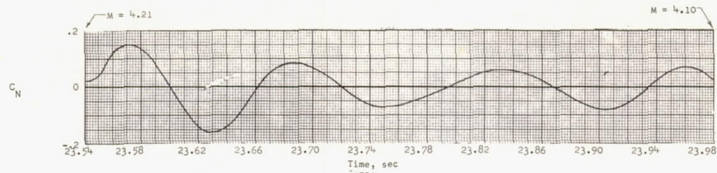
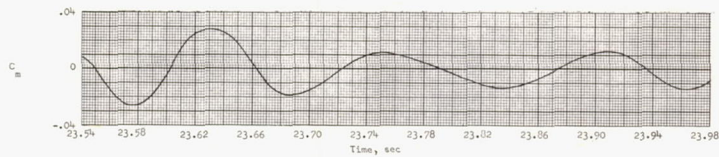


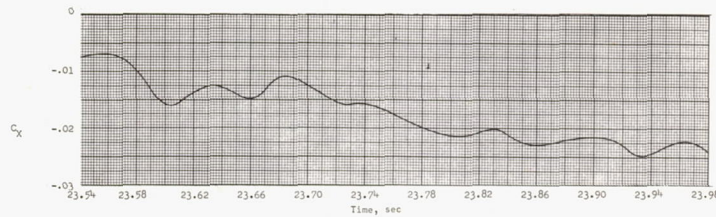
Figure 9.- Variation of amplitude and range of rolling velocity for free-flight model.



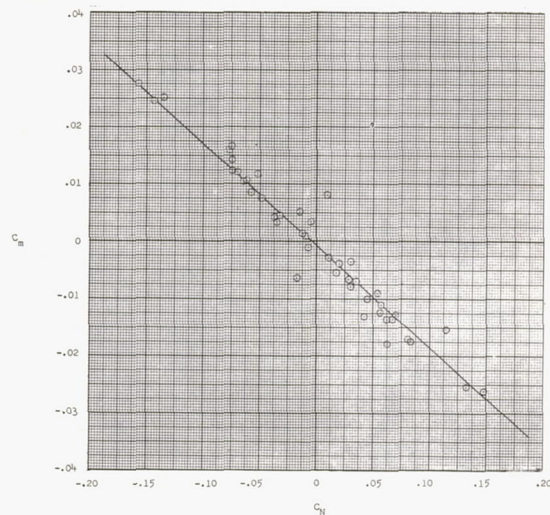
(a) Total normal-force coefficient.



(b) Total pitching-moment coefficient.



(c) Total axial-force coefficient. Pulse-rocket ignition occurred at 23.52 seconds.

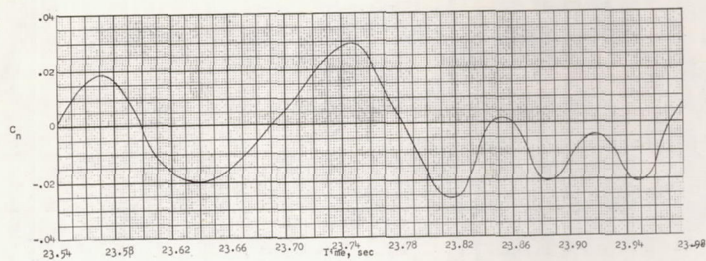


(d) Variation of C_m with C_N .

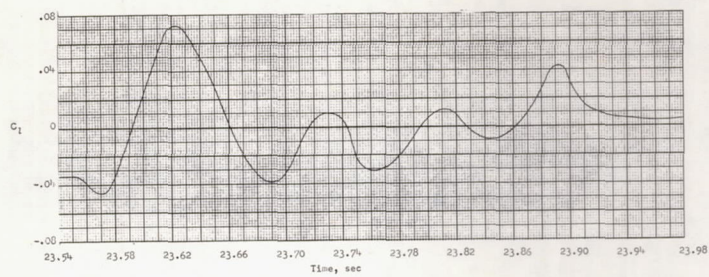
Figure 10.- Time histories of total force and moment coefficients along with cross plots of pitch and yaw coefficients. $M \approx 4.1$.



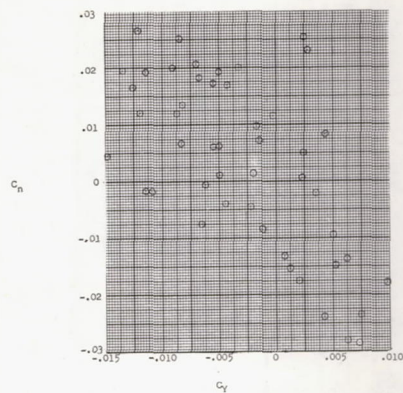
(e) Total side-force coefficient.



(f) Total yawing-moment coefficient.

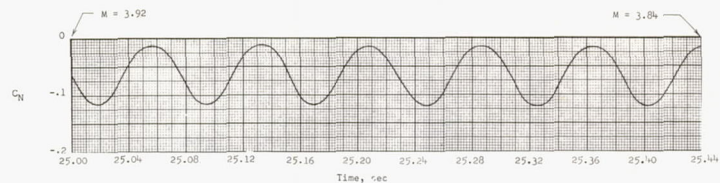


(g) Total rolling-moment coefficient

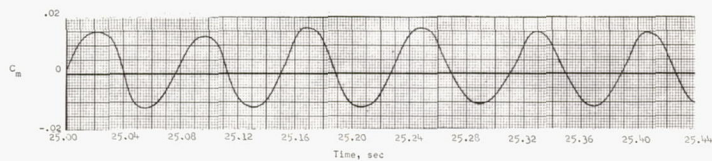


(h) Variation of C_n with C_y .

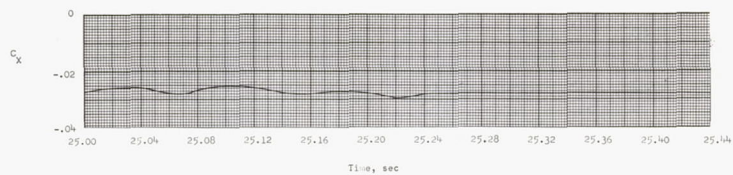
Figure 1C.- Concluded.



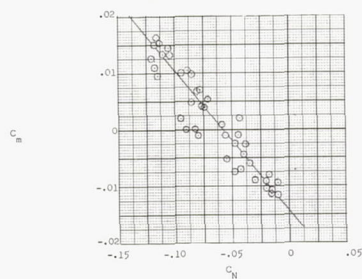
(a) Total normal-force coefficient.



(b) Total pitching-moment coefficient.

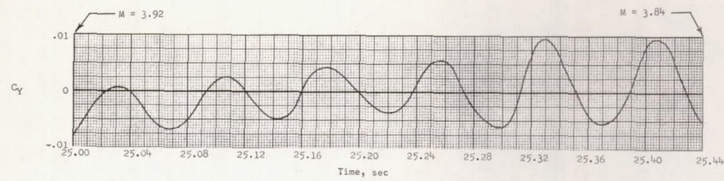


(c) Total axial-force coefficient.

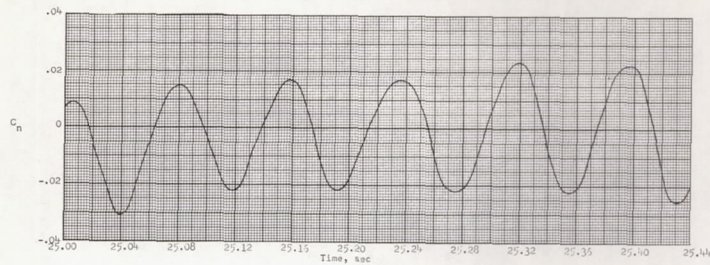


(d) Variation of C_m with C_N .

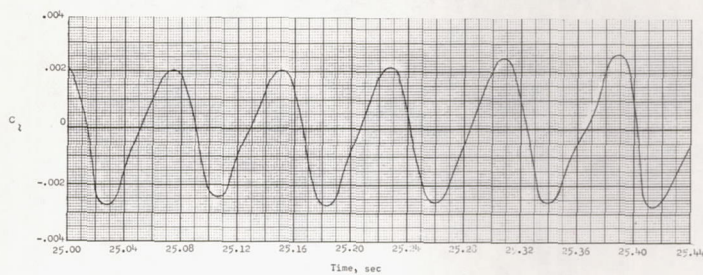
Figure 11.- Time histories of total force and moment coefficients along with cross plots of pitch and yaw coefficient. $M \approx 3.9$.



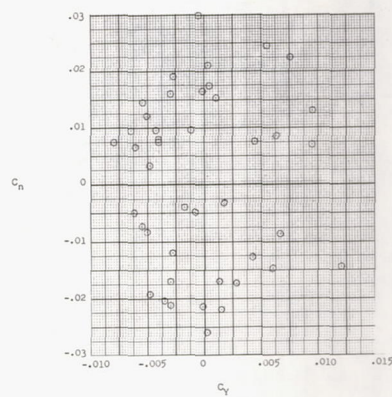
(e) Total side-force coefficient.



(f) Total yawing-moment coefficient.

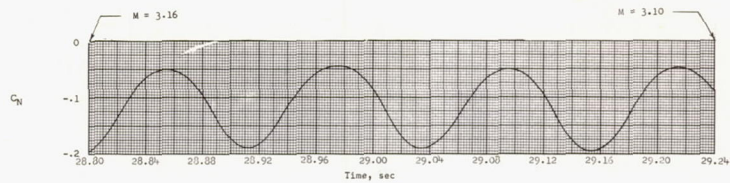


(g) Total rolling-moment coefficient.

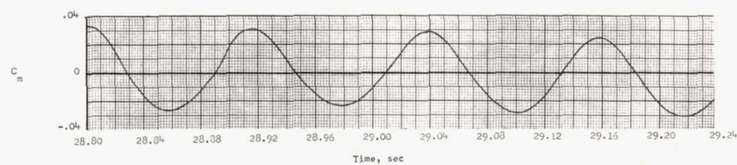


(h) Variation of C_n with C_Y .

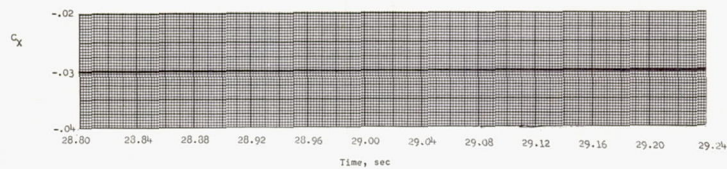
Figure 11.- Concluded.



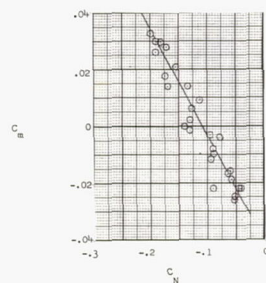
(a) Total normal-force coefficient.



(b) Total pitching-moment coefficient.

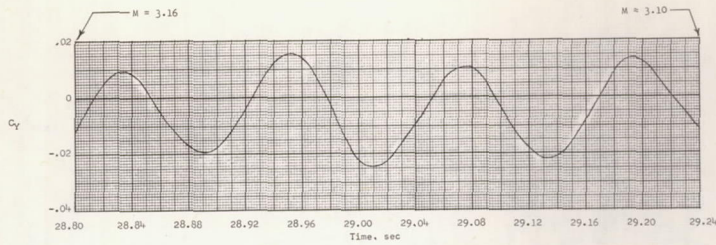


(c) Total axial-force coefficient.

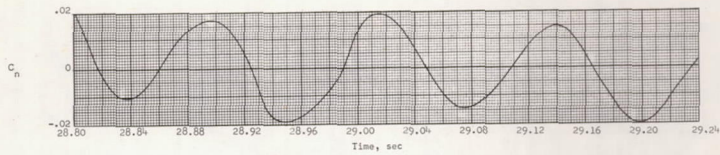


(d) Variation of C_m with C_N .

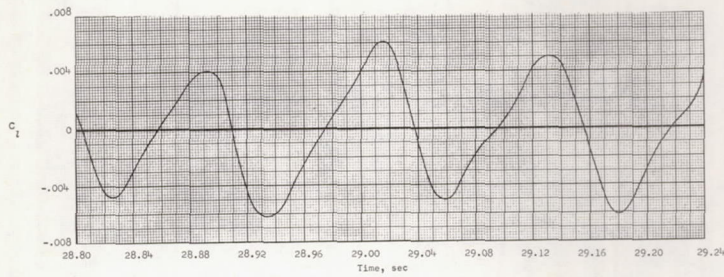
Figure 12.- Time histories of total force and moment coefficients along with cross plots of pitch and yaw coefficients. $M \approx 3.1$.



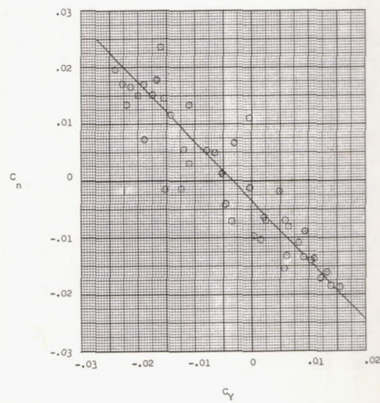
(e) Total side-force coefficient.



(f) Total yawing-moment coefficient.

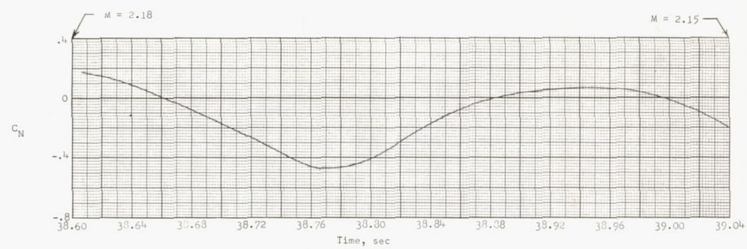


(g) Total rolling-moment coefficient.

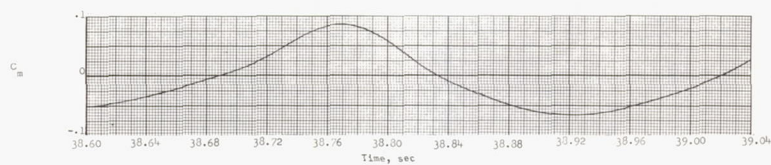


(h) Variation of C_n with C_Y .

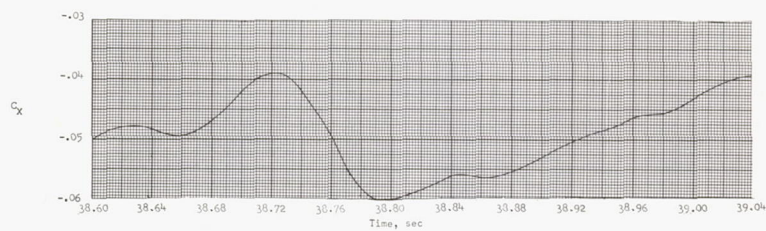
Figure 12.- Concluded.



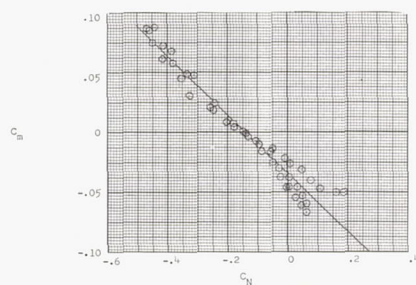
(a) Total normal-force coefficient.



(b) Total pitching-moment coefficient.

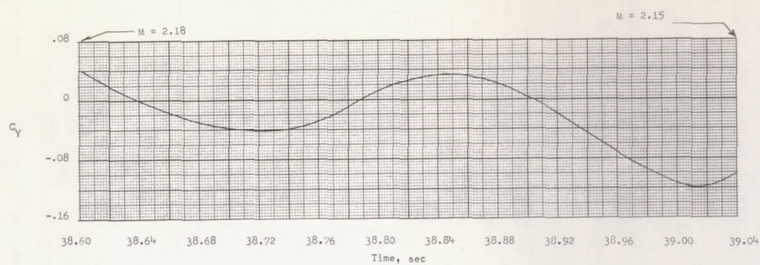


(c) Total axial-force coefficient.

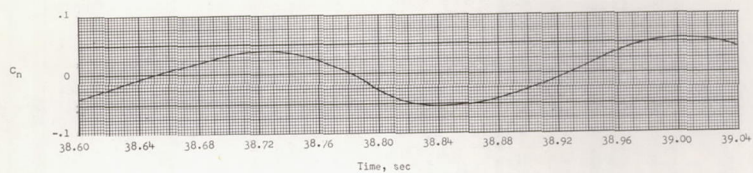


(d) Variation of C_m with C_N .

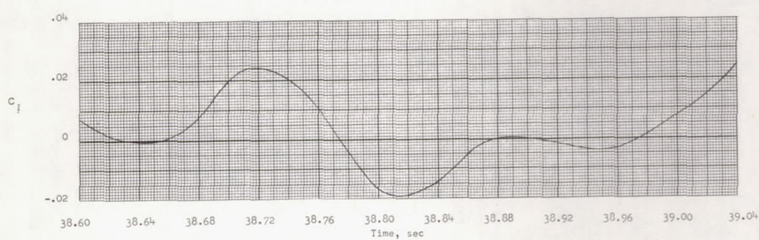
Figure 13.- Time histories of total force and moment coefficients along with cross plots of pitch and yaw coefficients. $M \approx 2.1$.



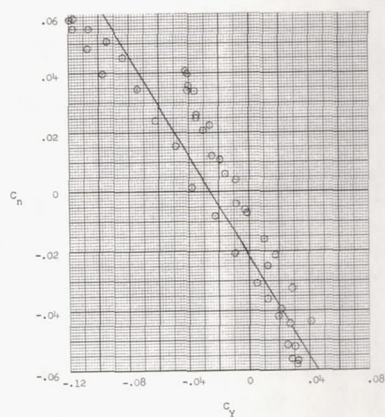
(e) Total side-force coefficient.



(f) Total yawing-moment coefficient.



(g) Total rolling-moment coefficient.



(h) Variation of C_N with C_Y .

Figure 13.- Concluded.

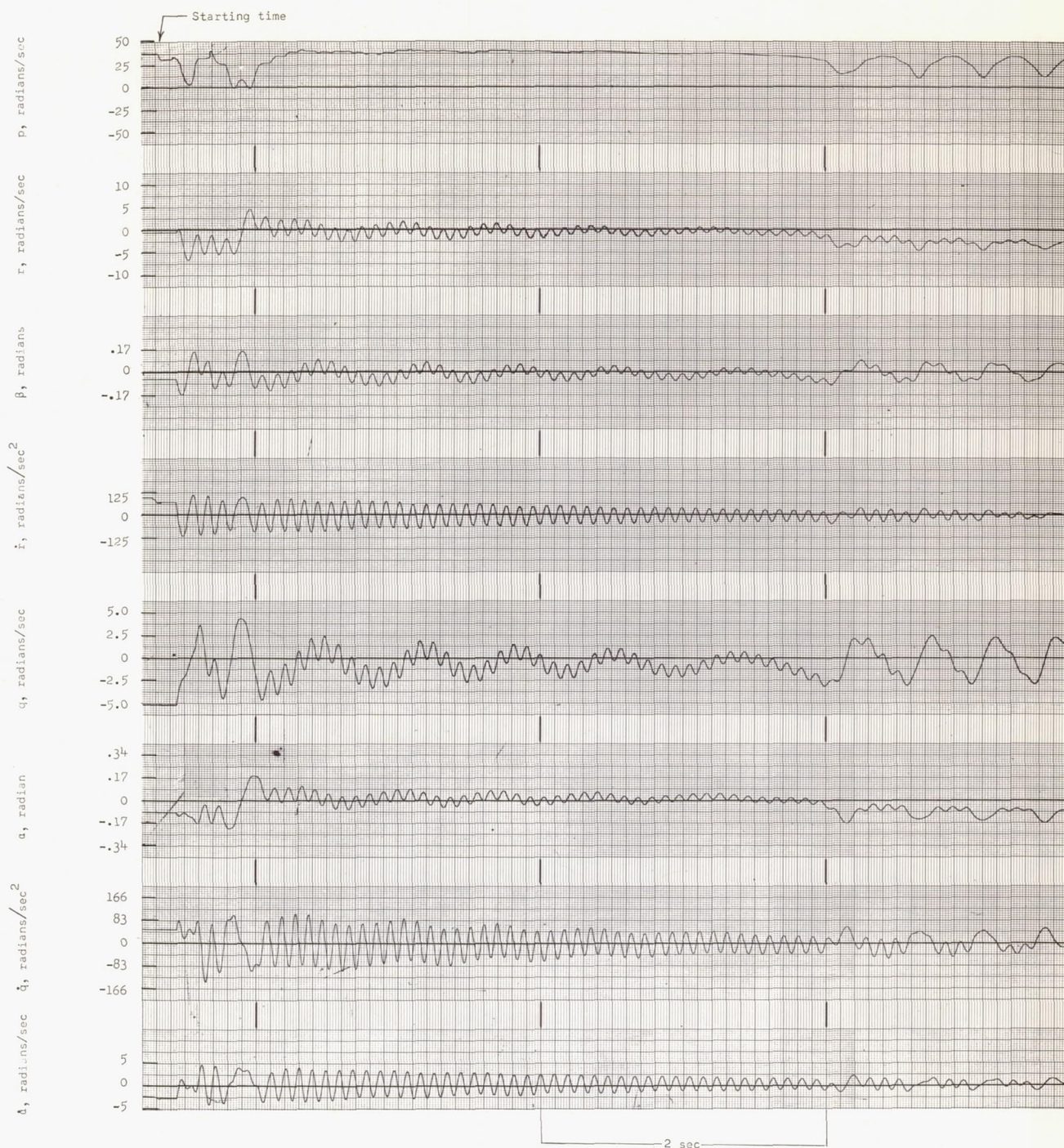


Figure 14.- Five-degree-of-freedom analog analysis record at $M = 4$.

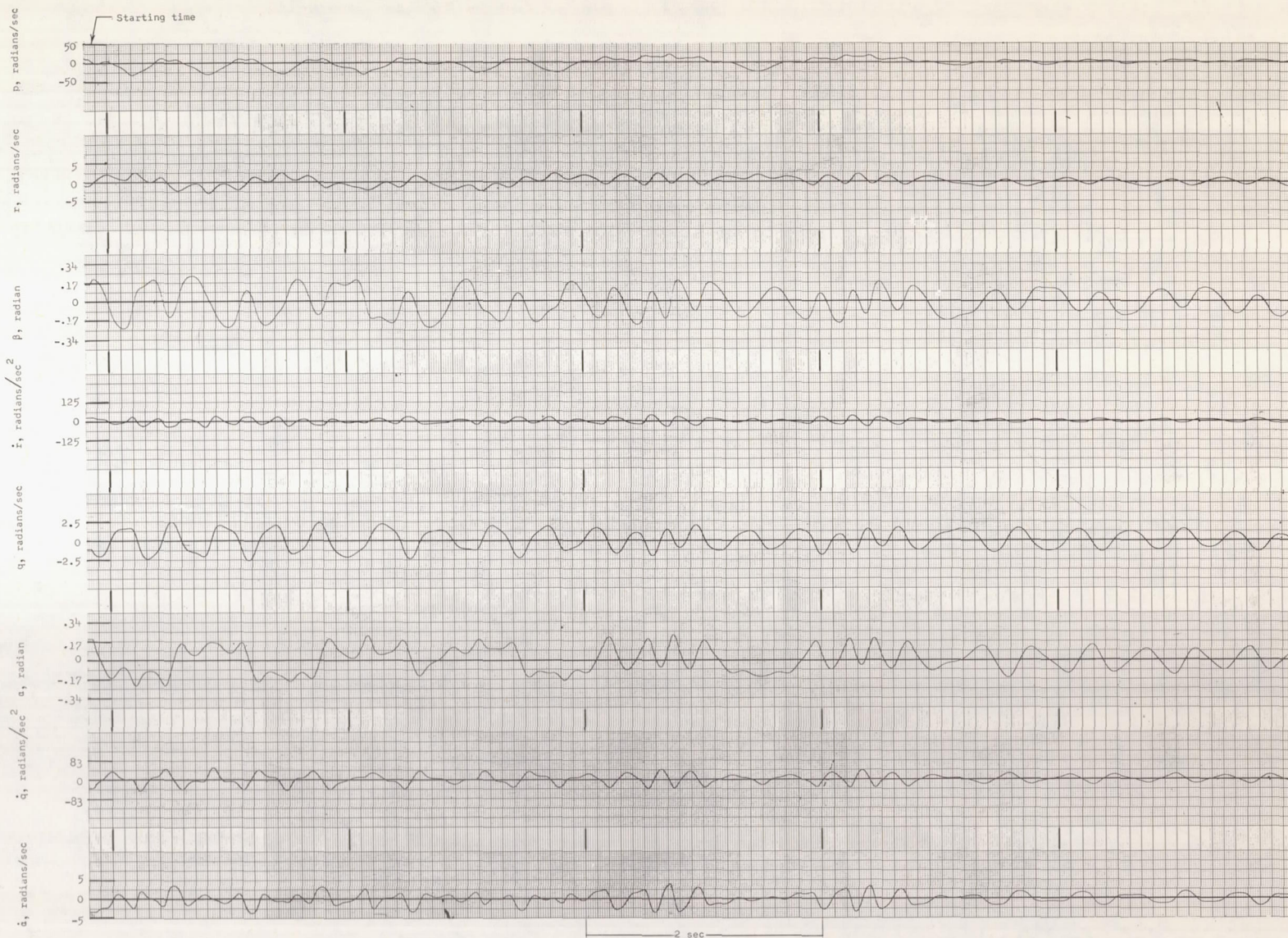


Figure 15.- Five-degree-of-freedom analog analysis record at $M = 2$.

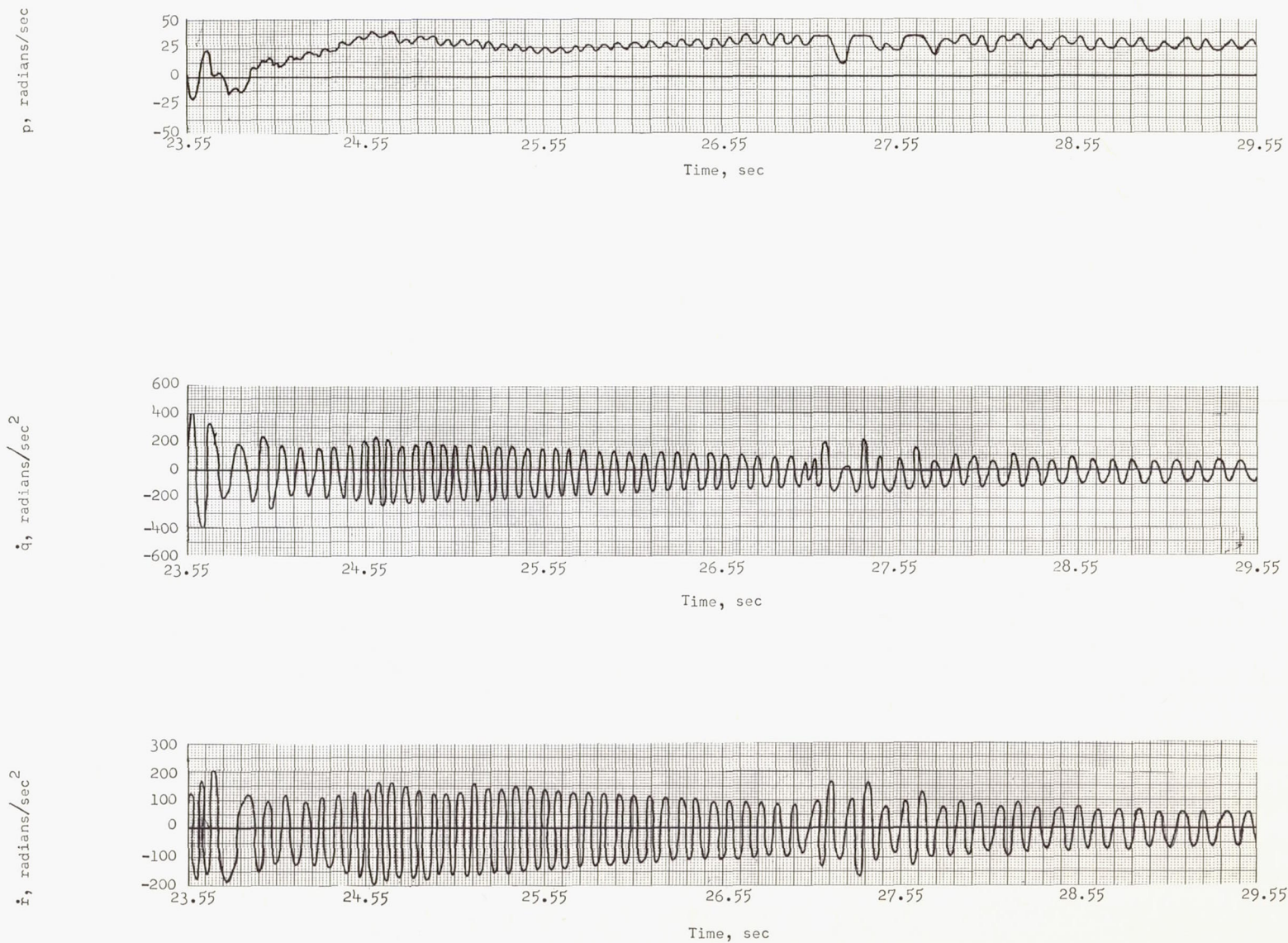


Figure 16.- Flight records at $M = 4$ of model roll rate and pitch and yaw accelerations.

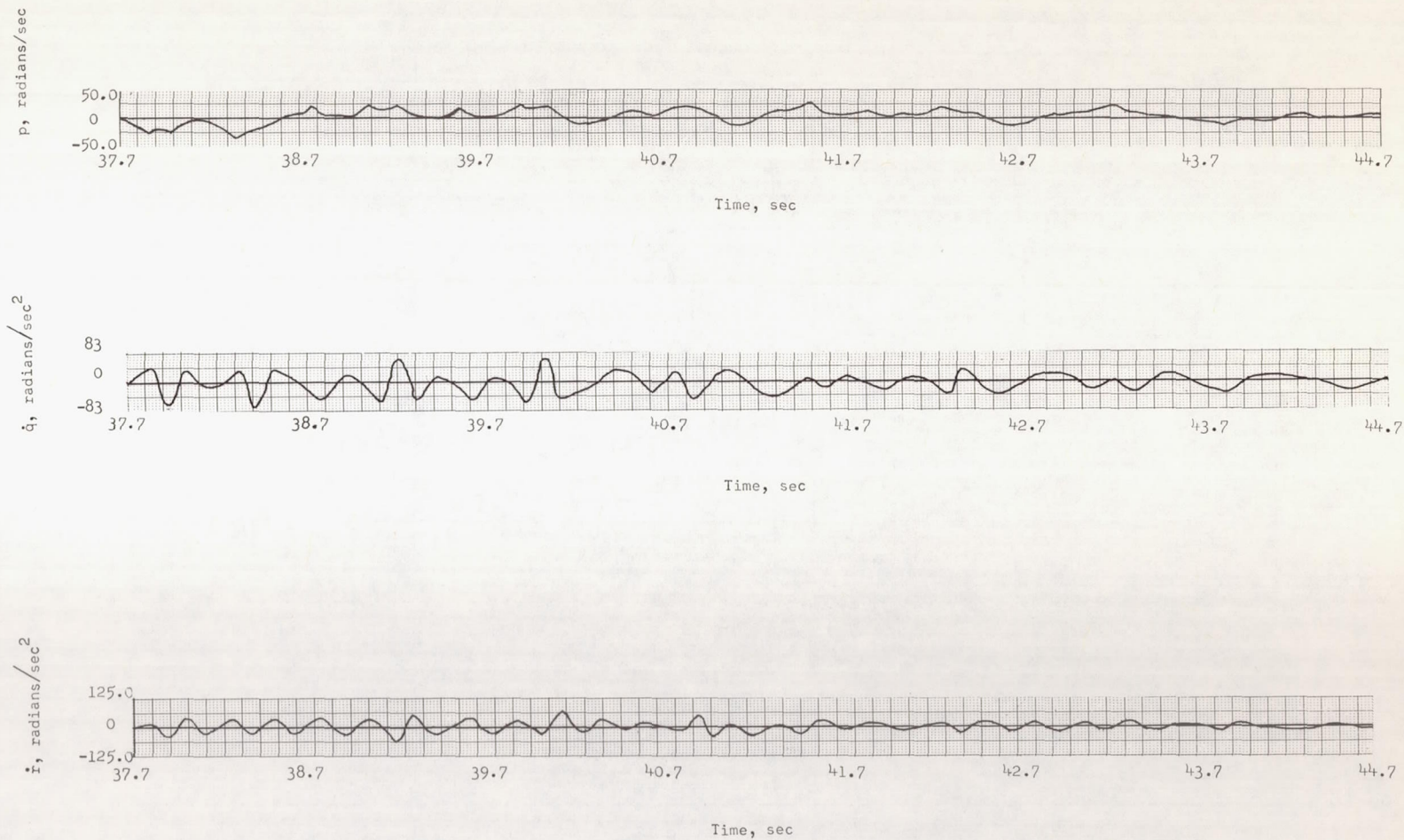


Figure 17.- Flight records at $M = 2$ of model roll rate and pitch and yaw accelerations.

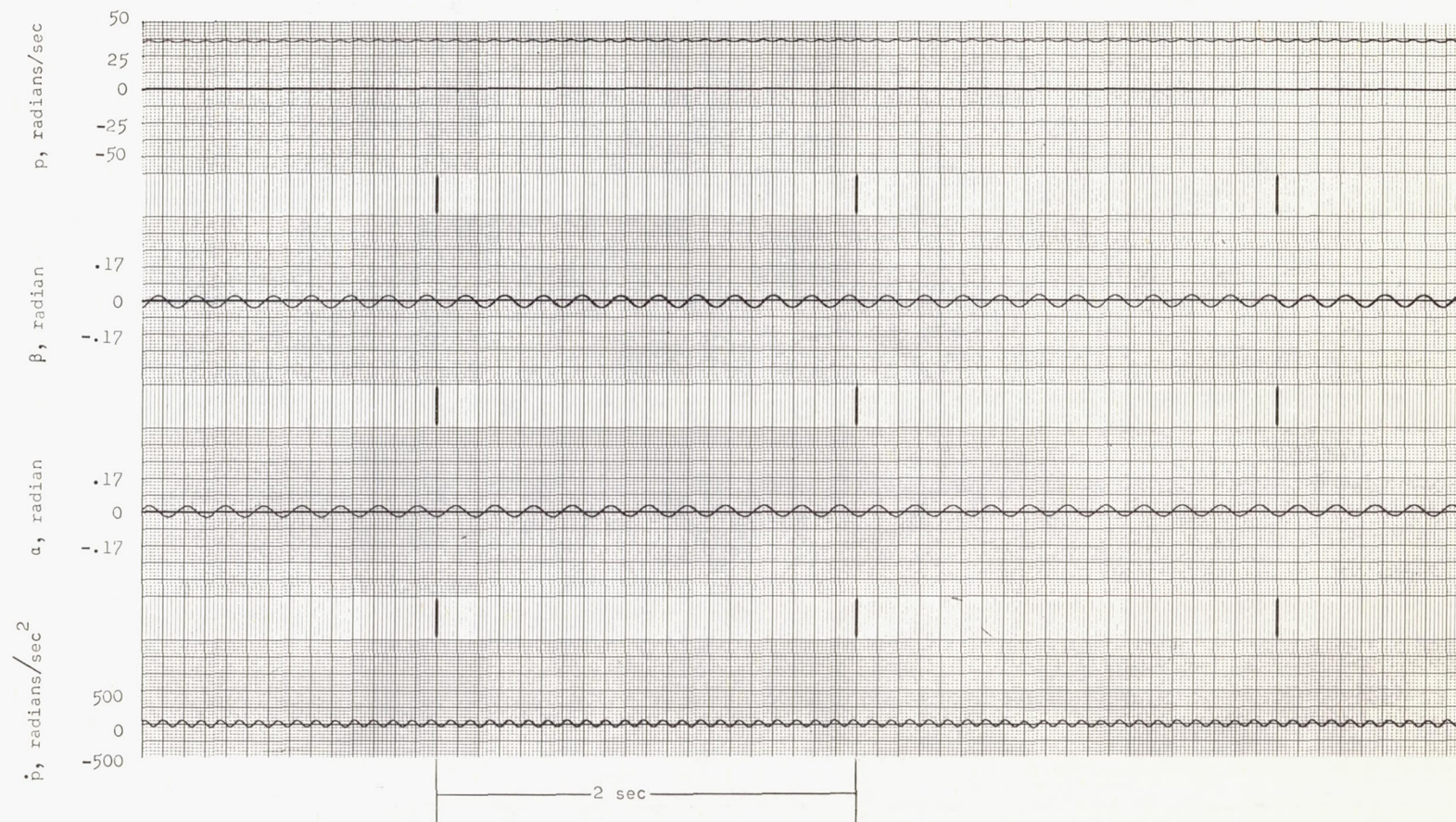


Figure 18.- Simplified analog analysis record at $M = 4$.

p , radians/sec

α , radians

β , radians

\dot{p} , radians/sec²

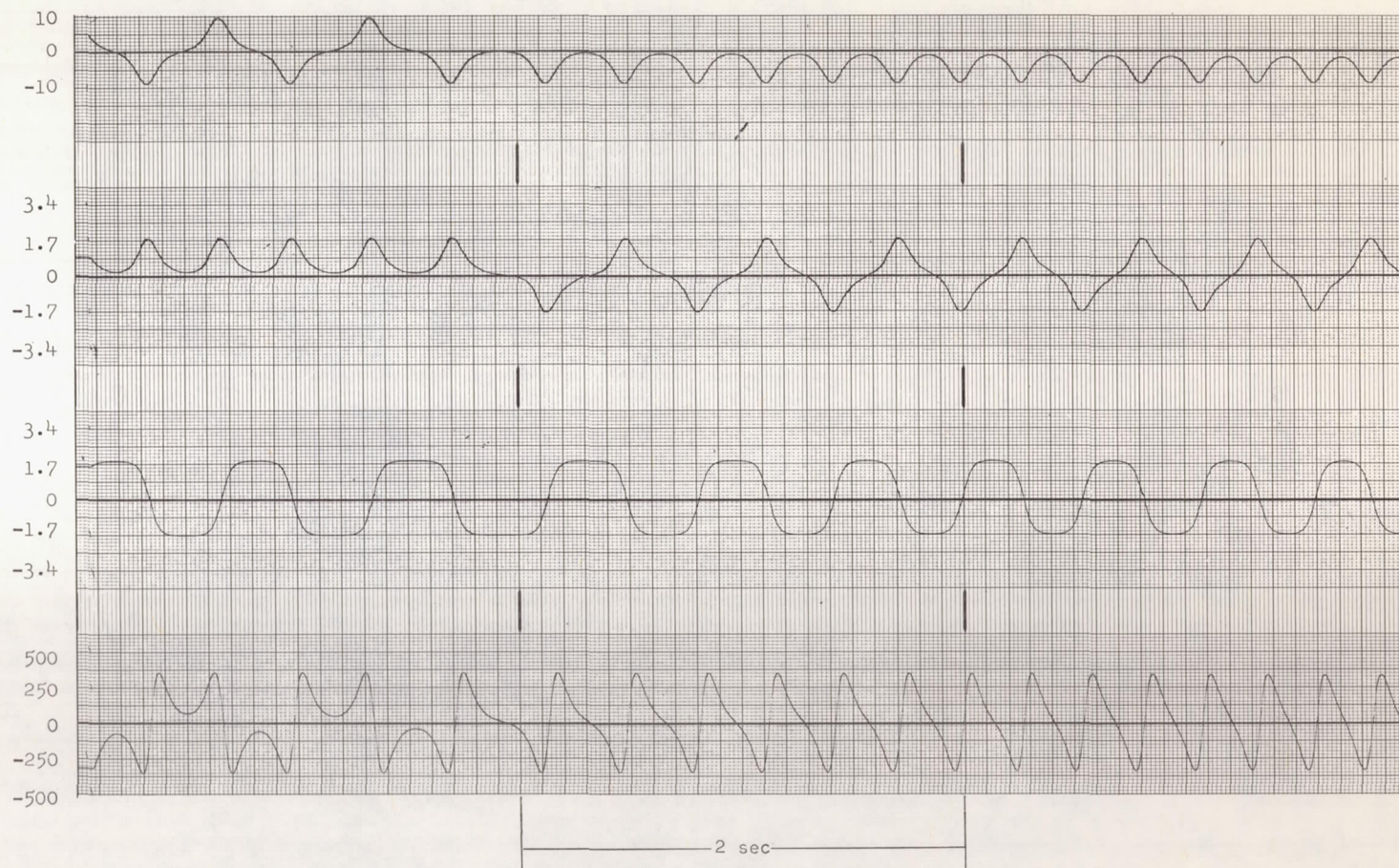


Figure 19.- Simplified analog analysis record at $M = 2$.

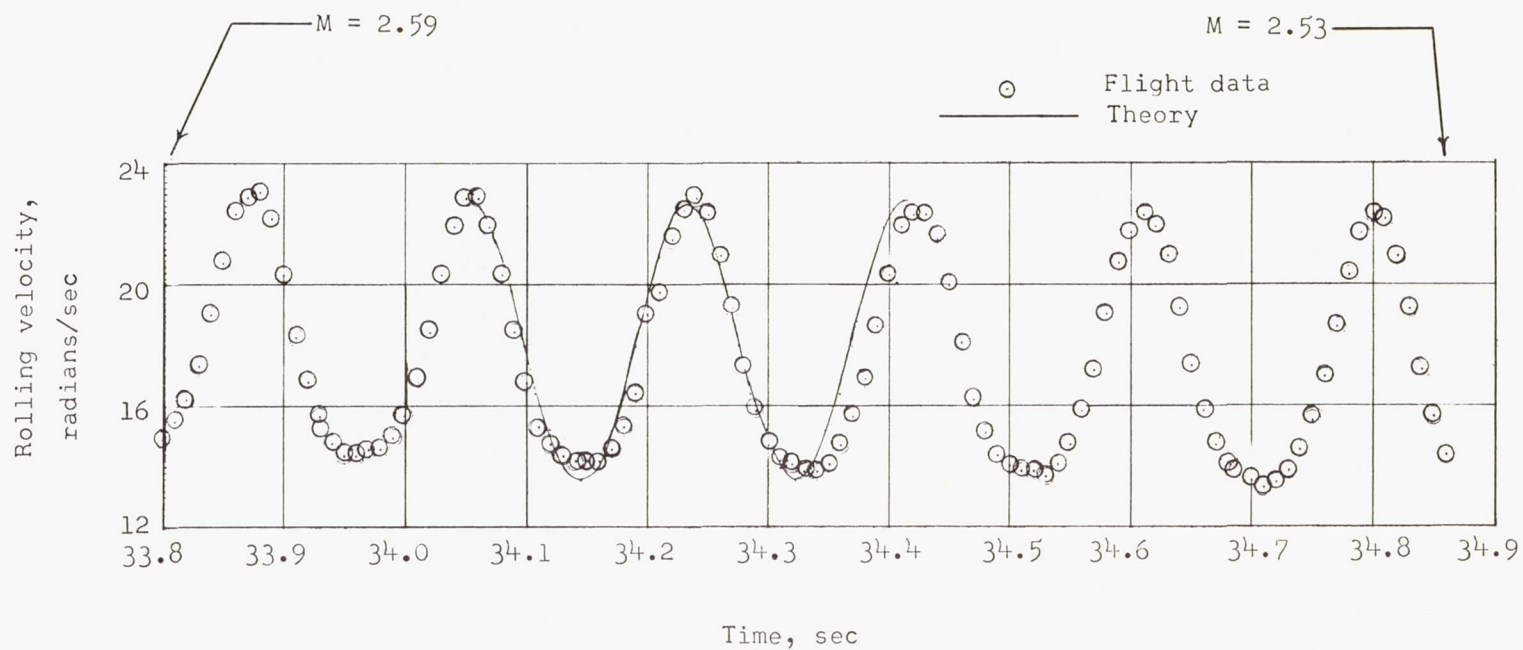


Figure 20.- Comparison of flight data and theory for variation of rolling velocity with time. $k = 0.80$.

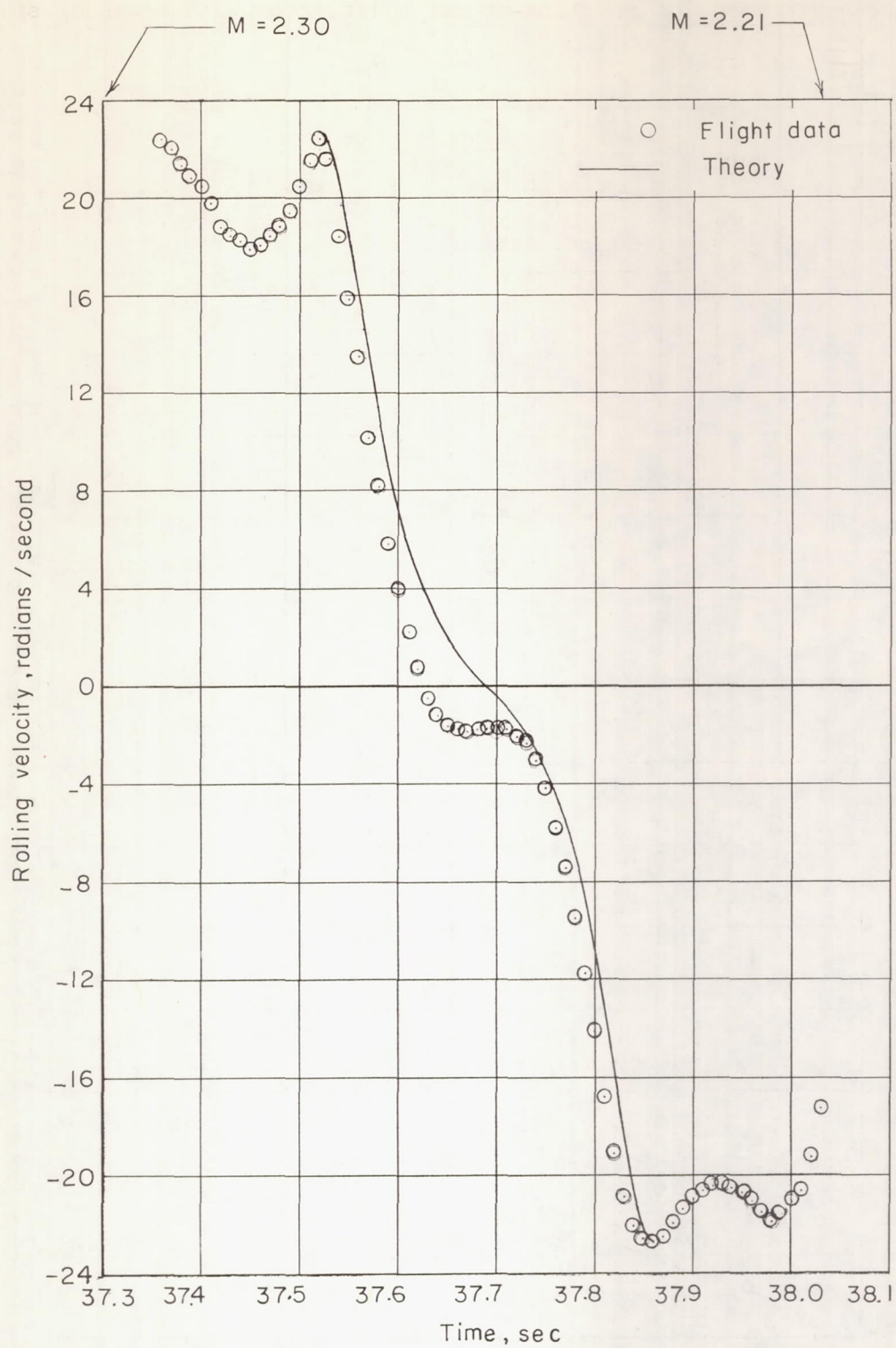


Figure 21.- Comparison of flight data and theory for variation of rolling velocity with time. $k = 1.004$.

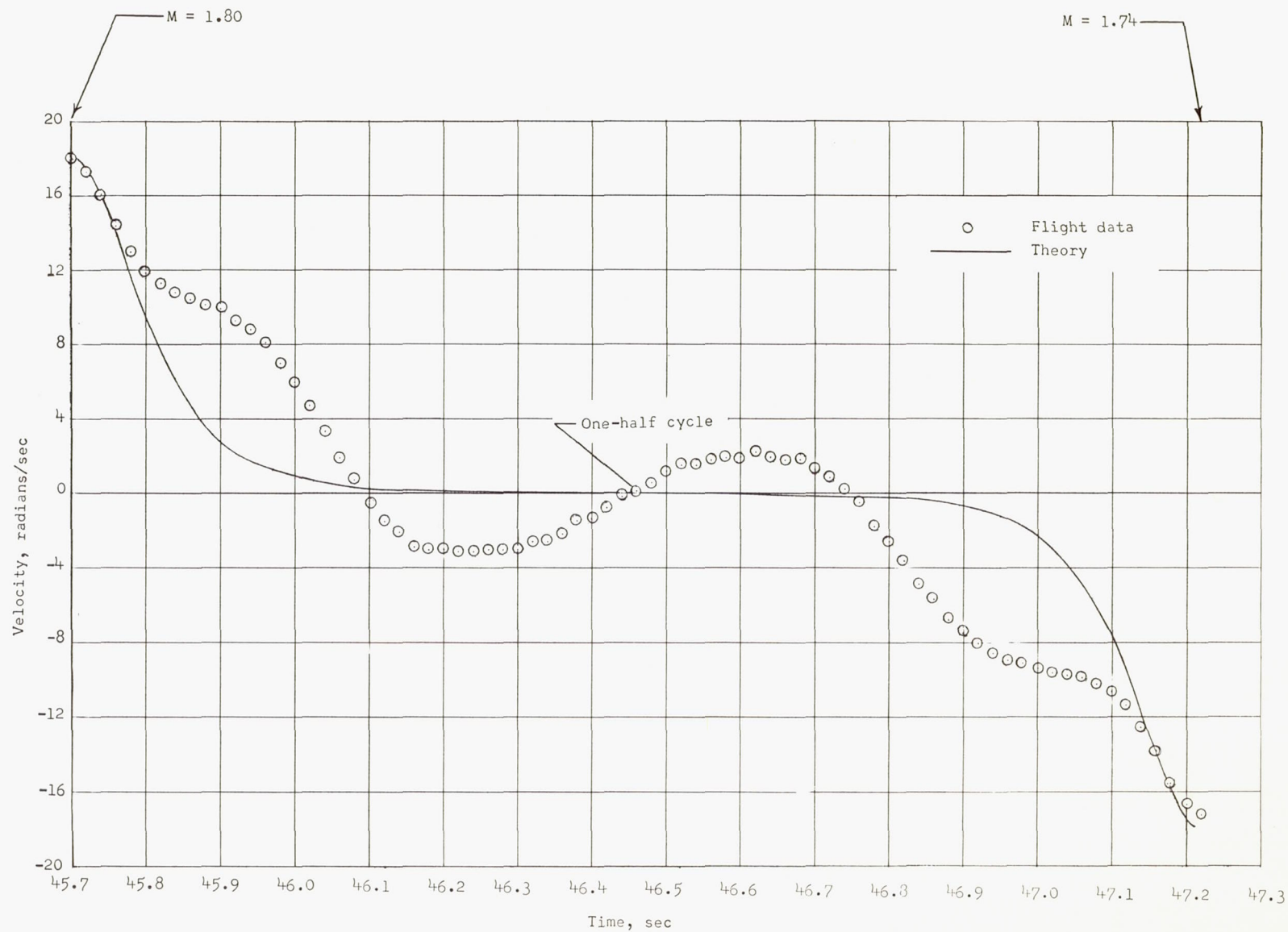


Figure 22.- Comparison of flight data and theory for variation of rolling velocity with time. $k = 1.0$.